Published in final edited form as:

J Immunol. 2015 March 15; 194(6): 2796–2809. doi:10.4049/jimmunol.1402210.

SHP-1-dependent macrophage differentiation exacerbates virus-induced myositis

Neva B. Watson[*], **Karin M. Schneider**[*], and **Paul T. Massa**[*,†]

[*]Department of Microbiology & Immunology, SUNY Upstate Medical University, Syracuse, NY 13210

[†]Department of Neurology, SUNY Upstate Medical University, Syracuse, NY 13210

Abstract

Virus-induced myositis is an emerging global affliction that remains poorly characterized with few treatment options. Moreover, muscle-tropic viruses often spread to the central nervous system causing dramatically increased morbidity. Therefore, there is an urgent need to explore genetic factors involved in this class of human disease. This report investigates critical innate immune pathways affecting murine virus-induced myositis. Of particular importance, the key immune regulator SHP-1, which normally suppresses macrophage-mediated inflammation, is a major factor in promoting clinical disease in muscle. We show that Theiler's murine encephalomyelitis virus infection of skeletal myofibers induces inflammation and subsequent dystrophic calcification with loss of ambulation in wild type mice. Surprisingly, although similar extensive myofiber infection and inflammation is observed in SHP-1-deficient (SHP-$1^{-/-}$) mice, these mice neither accumulate dead calcified myofibers nor lose ambulation. Macrophages were the predominant effector cells infiltrating WT and SHP-$1^{-/-}$ muscle, and an increased infiltration of immature monocytes/macrophages correlated with absence of clinical disease in SHP-$1^{-/-}$ mice, while mature M1-like macrophages corresponded with increased myofiber degeneration in WT mice. Furthermore, blocking SHP-1 activation in WT macrophages blocked virus-induced myofiber degeneration, and pharmacologic ablation of macrophages inhibited muscle calcification in TMEV-infected WT animals. These data suggest that following TMEV infection of muscle, SHP-1 promotes M1 differentiation of infiltrating macrophages, and these inflammatory macrophages are likely involved in damaging muscle fibers. These findings reveal a pathological role for SHP-1 in promoting inflammatory macrophage differentiation and myofiber damage in virus-infected skeletal muscle, thus identifying SHP-1 and M1 macrophages as essential mediators of virus-induced myopathy.

Introduction

Prevalent human single-stranded RNA viruses including retroviruses, flaviviruses, alphaviruses, picornaviruses and rhabdoviruses are commonly associated with skeletal

Paul T. Massa, Tel: 315-464-7606, Fax: 315-464-4417, Massap@upstate.edu

Disclosures

The authors have no conflicting financial interests.

muscle infection and inflammation resulting from either direct infection of myofibers or infiltrating inflammatory macrophages (1–15). As a consequence of these infections, spreading of the virus from muscle to CNS by retrograde axonal transport or viremia may occur causing severe neuropathological complications (16–20). Skeletal muscle is therefore a clinically significant target of virus infections in humans and the mechanisms involved in this process must be further elucidated.

Among the most clinically relevant muscle-tropic viruses, arthropod-borne RNA viruses (arboviruses) including flaviviruses and alphaviruses are emerging disease threats worldwide in both developing and developed nations, and these infections are associated with a high incidence of neurological manifestations (21). Alphaviruses such as Ross River virus, Chikungunya virus and Sindbis virus have been demonstrated to trigger debilitating muscle and CNS disease in humans and mice, and skeletal muscle fibers have been described as targets for initial replication in the periphery (22–29). Moreover, recent studies have suggested that disease severity of Chikungunya virus strains can be predicted by the ability of each strain to infect myofibers (30, 31). It is therefore common that muscle serves as an initial target for neurotropic viruses.

Another important aspect of these virus-induced neuromuscular diseases is the particular targeting of children. Many childhood viral infections trigger central nervous system (CNS) disease and/or muscle dysfunction, with severe cases of muscle involvement manifesting in severe inflammatory myositis and/or rhabdomyolysis (32–35). Thus, virus infections involving skeletal muscle with common subsequent neurological involvement is an escalating clinical problem with increased predilection for children. Therefore, defined animal models for these infections are needed to study genetic and immune mechanisms at play in the development of severe virus-induced muscle and subsequent CNS disease.

Theiler's murine encephalomyelitis virus (TMEV) is a neurotropic picornavirus belonging to the cardiovirus genus that is comprised of two subgroups (36). GDVII, the highly virulent strain, causes an acute paralytic disease with infection of neurons in the brain and spinal cord leading to encephalitis and death. GDVII has additionally been reported to induce myositis marked by extensive myofiber necrosis following intramuscular inoculation (36–38). In contrast, attenuated strains of TMEV including BeAn and DA are only neurotropic when inoculated intracranially into susceptible strains of adult mice (36). These attenuated strains of TMEV are commonly used as a virus-induced model of multiple sclerosis, often causing subclinical neuronal infection followed by persistence in glia and inflammatory demyelination weeks to months after infection (36). Importantly, attenuated TMEV strains have been demonstrated to induce a severe acute myositis following intramuscular inoculation and induce an immune cell-mediated acute myositis following intraperitoneal (IP) inoculation into several strains of suckling mice (38, 39). These studies indicate that TMEV infection of suckling mice may provide a model system for studying the pathogenesis of virus-induced muscle disease that may be relevant for increased childhood susceptibility to these viruses.

We have previously established that suckling SHP-1-deficient mice (motheaten, me/me) suffer CNS disease following intracranial or peripheral infection with the attenuated BeAn

strain of TMEV, while wild type (WT) mice are resistant to this disease (40–42). In this model, macrophages were found to mediate TMEV-induced demyelination in SHP-$1^{-/-}$ mice, as blocking macrophage infiltration inhibited TMEV infection of the CNS, corresponding with reduced disease severity (40, 41). SHP-1 (Src homology region 2 domain-containing phosphatase 1) is a cytosolic protein tyrosine phosphatase expressed predominantly in hematopoietic cells and functions as a key regulator of many cellular processes of innate immune cells, especially in macrophages (43, 44). In particular, SHP-1 controls essential monocyte/macrophage functions that are relevant to virus-induced inflammatory responses in tissues including transendothelial migration, adhesion, activation, polarization and phagocytic activity (44–46).

Presently, we report that both wild type and me/me suckling mice develop widespread myofiber infection and innate inflammatory responses in skeletal muscles upon peripheral inoculation with TMEV. However, TMEV induces severe myositis with impaired locomotion following peripheral inoculation of only wild type mice, while mice lacking SHP-1 are surprisingly resistant to this clinical muscle pathology. In particular, an accumulation of degenerating fibers and corresponding dystrophic fiber calcification was observed in WT but not SHP-1-deficient mice. Importantly, while TMEV infection of wild type and me/me muscle induces a pronounced infiltration of macrophages, there are clear differences in the phenotype of these cells between wild type and me/me mice that relate to striking differences in clinical muscle pathology. Of particular note, muscle pathology in wild type animals was coincident with macrophage differentiation toward an M1 phenotype, while muscle-infiltrating macrophages displayed a relatively immature phenotype in me/me mice. Additionally, TMEV genomes were much higher in wild type compared to me/me macrophages suggesting that an M1 differentiation program supported virus replication in these cells within muscle. Furthermore, blocking SHP-1 activation in wild type mice via the CD47-SIRPα-SHP-1 pathway blocked the development of both myofiber calcification and impaired ambulation. Finally, depleting macrophages in WT animals with clodronate liposomes inhibited the development of TMEV-induced muscle fiber degeneration and calcification. Thus, these findings demonstrate that SHP-1 plays a critical role in promoting M1 differentiation in virus-infected muscle and in promotion of debilitating virus-induced myositis.

Materials and Methods

Animals

SHP-1-deficient motheaten (me/me, C3FeLe.B6 *a*/*a*-*Ptpn6*^{me}/J) or viable motheaten (me^{v}/me^{v}, C57BL/6J–*Ptpn6*$^{me\text{-}v}$/J) mice, heterozygous and wild type littermates were produced from heterozygous breeding pairs obtained from The Jackson Laboratory (Bar Harbor, Maine; No. 000225 and 000811, respectively). Appropriate genotypes of all mice were verified commercially from tail DNA (Transnetyx, Inc. Cordova, TN). All animal experiments were performed under approval from the Institutional Animal Care and Use Committee (IACUC) at SUNY Upstate Medical University.

Infections

BeAn TMEV was obtained from ATCC (Manassas, VA; No. VR-995) and propagated within BHK-21 cells (ATCC; No. CCL-10). Plaque assays were performed to determine viral titer as plaque-forming units per milliliter (PFU/ml). 12 day old me/me mice and normal littermates were inoculated intraperitoneally with 100μl containing 6×10^6 PFU BeAn TMEV. Mice were monitored daily for signs of skeletal muscle disease (hunched, abnormal gait, swollen shoulders/hips). WT mice (n=16) were sacrificed upon clinical signs of muscle disease (9–15 days P.I.) unless otherwise noted, and development of skeletal muscle disease was further verified by presence of white calcified areas within skeletal muscle of mice upon dissection. Alternatively, WT and me/me littermates were sacrificed at 5 days P.I. and processed for RNA, histological and flow cytometry analysis.

12–14 day old me^v/me^v mice and normal littermates were inoculated intraperitoneally with 100μl containing 6×10^5 PFU – 3×10^6 PFU TMEV. Infections were independently repeated 5 times: one containing 3 me^v/me^v and 3 WT animals; once with 1 me^v/me^v and 2 WT animals; twice with 1 me^v/me^v and 5 WT animals; and once with 1 me^v/me^v and 1 WT animal, yielding 7 total me^v/me^v mice and 16 total WT littermates. Mice were monitored daily for signs of skeletal muscle disease (hunched, abnormal gait, swollen shoulders/hips). Mice were sacrificed upon clinical signs of muscle disease (7–15 days P.I.) unless otherwise noted. Development of skeletal muscle disease was further verified by presence of white calcified areas within skeletal muscle of mice upon dissection.

Histology

Skeletal muscle was dissected from the gluteus maximus muscle, snap frozen in OCT media (Sakura Finetek USA, Inc.; Torrance, CA) and stored at −80°C. 7μm sections were cut using a cryostat (Leica Microsystems CM1900, Wetzlar, Germany), air-dried and fixed with acetone (10 minutes at −20°C).

Sections for immunofluorescent stainings were blocked in 10% horse serum (Tissue Culture Biologicals, Tulare, CA; No. 601D) overnight at 4°C and incubated in 10% horse serum with primary antibodies overnight at 4°C. Rat anti-mouse Ly6c and F4/80 (BioLegend, San Diego, CA; No. 128001 and 123101) were diluted at 1:200, and rabbit antiserum against BeAn TMEV (a gift from Howard L. Lipton, University of Illinois at Chicago, Chicago, IL) was diluted at 1:2000. Fluorochrome-conjugated secondary antibodies (Dylight 488 donkey anti-rabbit and Dylight 594 goat anti-rat were obtained from Jackson ImmunoResearch Laboratories, Inc. (West Grove, PA; No. 711–545-152 and 112–515–167, respectively) and incubated for 2 hours at 4°C at a 1:500 dilution. DAPI (1μg/ml) was added for one minute and coverslips were mounted with fluorescence mounting medium (DAKO, Denmark; No. S3023).

H&E staining was performed with all steps at room temperature unless otherwise noted. Tissues were incubated with Harris's Hematoxylin (Sigma Diagnostics, St. Louis, MO; No. HHS-32) for 11 minutes in a slide-warmer (Lab-Line Instruments, Inc., Melrose Park, IL; No. 26025) at 50°C. Slides were decolorized with 0.3% HCl in 70% EtOH for approximately 50 seconds followed by an ammonium water wash (5 drops ammonium

hydroxide/100ml dH_2O) for 1 minute and stained with Eosin Y (Sigma Diagnostics; No. HT110-1–16) for 45 seconds. Slides were dried in a 50°C slide-warmer for 5 minutes and mounted with Permount (Electron Microscopy Sciences, Hatfield, PA; No. 17986-01).

Alizarin red S (Electron Microscopy Sciences; No. 26206-01) staining was performed on acetone-fixed sections according to the recommended manufacturer's protocol. Tissues were stained with Alizarin Red S for 2.5 minutes. Slides were dried on a 50°C slide-warmer and mounted with Permount.

Picrosirius red (Electron Microscopy Sciences; No. 26357-02) staining was performed on acetone-fixed sections according to the manufacturer's protocol. Phosphomolybdic acid was incubated for 5 minutes. Slides were dehydrated in EtOH, cleared in xylene and mounted with Permount.

Brightfield and fluorescent microscopy were performed using an Eclipse E800 microscope (Nikon, Tokyo, Japan) with a SPOT RT Slider digital camera (SPOT Imaging Solutions, Sterling Heights, MI). Images were obtained at 2×, 20× and 40× with numerical apertures of 0.06, 0.50 and 0.75, respectively, using Spot RT Software v3.0 (SPOT Imaging Solutions) at room temperature. Black and white fluorescent images were merged and pseudo-colored using ImageJ software (NIH; Bethesda, MD).

H&E cell counts were executed by placement of rectangles of a fixed area over representative regions of each tissue and counting cells within each area. Unit area for cell density within lesions was 2.25nm (30×75μm), and unit area for cells invading myofibers was 450μm (18×25μm). Areas were placed over two representative fields per tissue and averaged counts were analyzed for statistical significance.

Flow cytometry analysis

At 5 days post-infection all skeletal muscle was dissected from WT and me/me mice, including forearms, neck, back, hindlimbs and gluteus maximus muscles. Muscle was dissociated using a gentleMACS Dissociator and skeletal muscle dissociation kit (MACS Miltenyi Biotec, Cologne, Germany; No. 130-098–305) according to the manufacturer's protocol. Cells were passed through 40μm filters following red blood cell lysis. Cells were incubated at 4°C for 20 minutes in 2.4G2 supernatant (2.4G2 hybridoma line from ATCC; No. HB-197) to block CD16/32 Fcγ receptors. Cells were then stained for 30 minutes at 4°C with the following antibodies and concentrations diluted in 2.4G2 supernatant: CD45-PE (No. 103105, 1:100), CD11b–Pacific Blue (No. 101223, 1:800), Ly6c–Brilliant Violet 570 (No. 128030, 1:50), F4/80-PerCP/Cy5.5 (No. 123127, 1:50) or CCR2-APC (R&D Systems; Minneapolis, MN; No. FAB5538A, 1:10). Unless otherwise noted all antibodies were received from BioLegend. Flow cytometric analysis was performed using a BD LSR Fortessa cytometer with FACSDiva software (Becton Dickinson; San Jose, CA) and analyzed with FlowJo software (Tree Star Inc, Ashland, OR). Experiments were independently performed twice.

Fluorescence-activated cell sorting (FACS) was performed using a BD FACS Aria III cell sorter with FACSDiva software (Becton Dickinson; San Jose, CA) to isolate either muscle

or spinal cord-infiltrating cells for RNA analysis. Muscle-infiltrating cells were prepared as described above. To isolate spinal cord-infiltrating cells, whole spinal cords were dissected and dissociated using a gentleMACS dissociator and Neural Tissue Dissociation Kit according to the manufacturer's protocol (MACS Miltenyi Biotec; No. 130-092–628). Following red blood cell lysis myelin was removed from spinal cord cell suspensions using Myelin Removal Beads II (MACS Miltenyi Biotec; No. 130-096–733) according to the manufacturer's protocol. Muscle and spinal cord-infiltrating cells were labeled with CD45-PE, CD11b–Pacific Blue, Ly6c–Brilliant Violet 570 and F4/80-PerCP/Cy5.5. $CD45^+$ cells were gated and collected for spinal cords, and muscle cells were subsequently subjected to a generous $CD11b^+Ly6c^{+\ (hi\ and\ lo)}$ gate to yield $CD45^+CD11b^+Ly6c^+$ cells. 250,000 – 400,000 cells were collected per muscle sample, and 50,000 – 150,000 cells were collected per spinal cord. Cells were pelleted, suspended in RNA STAT-60 (Tel-Test, Inc., Friendswood, TX; No. Cs-111) and stored at −80°C until further processing for RNA extraction/analysis.

In vivo anti-CD47 treatment

Twelve WT C57BL/6 mice (The Jackson Laboratory; No. 00064) were inoculated with 6×10^6 PFU TMEV IP at 12 days. Mice were injected IP with 100μg Rat IgG2a, κ isotype control (BioLegend; No. 400516) or rat anti-CD47 antibodies (BioLegend; No. 400516 and 127512, respectively) every 2 days from 5 to 13 days P.I. and sacrificed at 16 days P.I. Four animals were used for each control and experimental group. Mice were observed daily for signs of disease and clinical disease scores were assigned according to the following rank scale: 1: hunched posture and ruffled fur; 2: swollen muscles/abnormal gait; 3: 1 limb immobilized; 4: 2 or more limbs immobilized; 5: death. Dissections and histological evaluation was performed as described above. This experiment was performed in duplicate.

Calcified area percentages of Alizarin red-stained muscle sections were quantified using ImageJ software (NIH). Brightfield images were converted to 8-bit files. Automatic threshold values were used to select and measure areas of calcified (pixelated) staining, threshold values were increased to select and measure entire tissue area, and percent of tissue calcification was calculated using these area measurements.

In vivo macrophage depletion

Ten WT C3H mice (C3FeLe.B6 *a*/*a*-*Ptpn6*^{me}/J strain) were inoculated with 6×10^7 PFU TMEV IP at 12 days. Mice were injected IP with 80μl containing 0.4mg clodronate or control liposomes (Clodrosome macrophage depletion kit, Encapsula Nano Sciences; Brentwood, TN; No. 8901) every 3 days from 6 to 12 days P.I. and sacrificed at 14 days P.I. Five animals received clodronate liposomes and five animals received control liposomes. Mice were observed daily for signs of disease and clinical disease scores were assigned according to the rank scale described above. Mice were observed for signs of muscle calcification upon dissection.

RNA analysis

Skeletal muscle was dissected from the gluteus maximus muscle, homogenized in RNA STAT-60 (Tel-Test, Inc.) and stored at −80°C. FACS-sorted cells were isolated for RNA

analysis as described above. Samples were further processed for RNA purification by phenol-chloroform extraction and RNAs were analyzed by custom designed Quantigene 2.0 Multiplex Assay (Affymetrix, Inc., Santa Clara, CA).

The Affymetrix QuantiGene Plex 2.0 Assay (a multiplex bead-based assay) was used to measure the expression of 41 genes of interest (including 38 target genes and 3 reference genes). Pre-validated probes for these genes were ordered directly from Affymetrix and arrived as a conjugated bead mixture. Mouse total RNA samples from muscle or cell-sorted samples were then processed with these probes according to the QuantiGene Plex 2.0 Assay Manual. Briefly, a working bead mix containing lysis mixture, blocking reagent, capture beads, and probe set was prepared and dispensed into the hybridization plate, and 20μl of total RNA containing 500ng (from muscle samples), 300ng (from muscle-sorted cells) or 50ng (from spinal cord-sorted cells) was added to each well. Background control wells received 20μl of water added to the bead mix. The hybridization plate was sealed and placed into a VorTemp 56 shaking incubator (Fisher) for 22 hours at 54°C and 600RPM.

After hybridization, the wash solution, pre-amplifier, amplifier, label probe, and streptavidin-phycoerythrin (SAPE) solutions were prepared according to the manual instructions. The hybridized samples were then transferred from the hybridization plate to the magnetic separation plate. Samples were washed using the Affymetrix Hand-Held Magnetic Plate Washer, and incubated sequentially for 1 hour each (50°C at 600RPM) with the pre-made amplifier solutions (pre-amplifier, amplifier, and label probe). The SAPE solution was then added to the plate and samples were incubated in the dark at room temperature for 30 minutes at 600RPM. Unbound SAPE was removed away using the SAPE Wash Buffer from the QuantiGene Plex Kit. Then, 130μl of SAPE Wash Buffer was added to each sample, and the plate was shaken at room temperature for 3 minutes at 800RPM to resuspend the beads. The plate was read immediately using the BioRad BioPlex 200 instrument using settings of 100ul volume; 60 seconds timeout; and 100 Bead Events/Bead region.

Fluorescent readings from blank wells were subtracted from fluorescent values for each mRNA of interest. Values exceeding background were then normalized to the geometric mean signal derived from three reference genes in each sample: Glyceraldehyde-3-phosphate dehydrogenase (GAPDH), Hypoxanthine-guanine phosphoribosyltransferase (HPRT1) and TATA binding protein 1 (TBP1). These normalized ratios were then scaled to positive integer values by multiplying them by a constant (10,000). Significant differences between sample groups were evaluated using a one-tailed unpaired t-test.

Statistical Analyses

GraphPad Prism 5 software was used to perform statistical analyses. One-tailed unpaired t tests were performed to compare one measurement between two groups, two-way ANOVAs with Bonferroni post hoc tests for multiple comparisons were performed to measure significant differences between means +/− SEM, and one-tailed Wilcoxon matched-pairs signed rank tests were performed to compare clinical disease scores between two groups. P values are as follows: * = $p < 0.05$, ** = $p < 0.01$, *** = $p < 0.001$ and **** = $p < 0.0001$.

GraphPad Prism 5 software was additionally used to calculate statistical significance of disease incidence using two-sided Fisher's exact test.

Results

TMEV-induced skeletal muscle disease in wild type mice

We have previously reported that suckling mice lacking SHP-1 (me/me) on a C3H background develop rapid central nervous system (CNS) inflammatory disease following intraperitoneal inoculation of the attenuated BeAn TMEV strain within 5–8 days P.I. (40). Although wild type animals remain free of CNS disease, we observed that IP inoculation of TMEV in suckling heterozygous and homozygous wild type littermates produced a severe debilitating disease of the skeletal muscle between 9–15 days P.I. (Figure 1, Table 1). As no phenotypic difference between heterozygous and homozygous wild type littermates was seen following infection we will refer to both +/− and +/+ animals as wild type in this report. Mice exhibiting TMEV-induced muscle disease suffered loss of limb function that was musculoskeletal rather than neurological in nature as clinical examination and dissection revealed exceptionally stiff, swollen skeletal muscle presenting a white appearance, with limbs completely immobilized in severe cases (Figure 1). Experiments utilizing WT mice on a BL/6 background demonstrated that TMEV triggered comparable muscle pathologies in both C3H and BL/6 mice (Figure 1), signifying that TMEV-induced muscle disease was not specific to the C3H strain in agreement with previous studies (39). Muscle pathology was absent in both mock-injected BL/6 and C3H mice (Figure 1, BL/6 not shown).

To determine the pathological basis for this phenotype, hematoxylin and eosin (H&E) and alizarin red stains were performed on serial skeletal muscle sections from infected mice. The white appearance of skeletal muscle in wild type mice was likely due to calcification as alizarin red staining was strongly positive (Figure 1). Moreover, calcification was restricted to degenerating myofibers suggesting that the process of calcification occurred primarily in fibers undergoing terminal degeneration that eventually led to fiber loss. Accompanying fibrosis was also prevalent as observed by picrosirius red staining (Figure 1), further supporting the notion of TMEV-induced dystrophic calcification of skeletal muscle.

Lack of TMEV-induced muscle disease in SHP-1-deficient mice

In contrast to wild type mice, no overt clinical or anatomical signs of TMEV-induced muscle disease were visible in SHP-1-deficient motheaten (me/me) mice. This suggested that SHP-1 might facilitate myofiber calcification and muscle pathology in wild type animals. However, as me/me mice succumb to CNS disease prior to the time at which muscle disease is clearly discernible in wild type mice, we performed similar experiments with viable motheaten (me^v/me^v) mice (BL/6 background) in which CNS disease develops later than me/me mice (42). As depicted in Figure 2 and Table 1, all BL/6 wild type mice exhibited signs of muscle calcification by 7 days after infection, while calcification was never observed in me^v/me^v littermates by the time the mice succumbed to CNS disease (up to 11 days after infection). Alizarin red stainings confirmed the presence of degenerating calcified myofibers in WT but not in me^v/me^v muscle (Figure 2B), further validating sharply reduced myofiber degeneration and muscle pathology in SHP-1-deficient mice. Although

me^{v}/me^{v} mice did not show signs of myofiber death/calcification, both me^{v}/me^{v} and WT littermates exhibited equal signs of muscle fibrosis at 9 days P.I. (Figure 2B) indicating that myofiber calcification was a specific marker of clinical disease in WT animals.

Phenotypic differences of infiltrating macrophages in WT and SHP-1$^{-/-}$ mice

A prominent feature of TMEV-infected muscle both before and during the development of clinical muscle pathology was the presence of extensive macrophage invasion into infected muscles of both SHP-1$^{-/-}$ and wild type mice (Figures 3 and 7), while an increased yet relatively low numbers of Ly6g^{+} cells were observed within SHP-1$^{-/-}$ compared to WT muscle by immunofluorescence and flow cytometry analysis (data not shown). As SHP-1 is expressed at high levels in monocytes/macrophages we reasoned that development of muscle pathology might be controlled by SHP-1 in these cells. Indeed, in both SHP-1$^{-/-}$ and wild type mice there was an extensive infiltration of predominantly Ly6c^{+} macrophages that were especially localized to regions of extensive TMEV-infected myofibers (examples of these regions depicted in Figure 3A). This observation suggested that macrophage infiltration in WT and SHP-1$^{-/-}$ muscle generally localized to areas of TMEV infection of myofibers. Although both genotypes contained abundant infiltrates, macrophage infiltration consistently appeared more robust in SHP-1$^{-/-}$ compared to wild type muscle (Figure 3A). To support this observation, the average densities of infiltrating cells accumulating between or within muscle fibers of infected SHP-1$^{-/-}$ and WT mice were enumerated. Cell counts revealed a higher density of inflammatory cells between myofibers of SHP-1$^{-/-}$ muscle compared to wild type (Figure 3B–C).

To extend the observation that muscle of SHP-1$^{-/-}$ mice displayed a more pronounced infiltration of inflammatory monocytes/macrophages in infected muscle, flow cytometry was performed on cells isolated from WT and me/me muscle at 5 days after infection. It is generally well understood that CD11b^{+}Ly6c^{hi}CCR2^{hi} inflammatory monocytes patrol the bloodstream and respond to damaged/inflamed tissues in an MCP-1-dependent manner, and upon entry into inflamed tissues such as skeletal muscle, inflammatory monocytes mature into macrophages first by downregulating CCR2 and subsequently downregulating Ly6c while gaining F4/80 expression (Figure 4A) (47–50). Therefore, we first enumerated infiltrating CD11b^{+}Ly6c^{hi} and CD11b^{+}Ly6c^{lo} cells within WT and me/me muscle, and CD45 was used as an initial gate to exclude non-hematopoietic cells. We observed significantly higher numbers of both infiltrating CD45^{+}CD11b^{+}Ly6c^{hi} and CD45^{+}CD11b^{+}Ly6c^{lo} cells per gram of muscle in SHP-1$^{-/-}$ compared to WT mice (Figure 4B). These data supported our histological observations, demonstrating a much more robust infiltration of both Ly6c^{hi} and Ly6c^{lo} monocyte-derived cells in SHP-1$^{-/-}$ compared to WT muscle.

To further evaluate potential phenotypic differences between infiltrating macrophages in WT compared to me/me mice we analyzed levels of the differentiation markers CCR2 and F4/80 on muscle-infiltrating macrophages by flow cytometry. The most striking differences observed were high levels of CCR2 expression on CD45^{+}CD11b^{+}Ly6c^{hi} cells in me/me compared to WT mice, and low levels of F4/80 expression on CD45^{+}CD11b^{+}Ly6c^{lo} macrophages in me/me compared to WT mice, as observed by contour plots (Figure 4C).

Consistent with this observation, $CD45^+CD11b^+Ly6c^{hi}F4/80^{lo}$ cells in me/me mice displayed a significantly increased CCR2 MFI, while $CD45^+CD11b^+Ly6c^{lo}CCR2^{lo}$ cells in me/me mice displayed a significantly decreased F4/80 MFI, compared to corresponding WT populations (Figure 4D). These observations suggested a role for SHP-1 in governing macrophage maturation following recruitment of $Ly6c^{hi}CCR2^{hi}$ inflammatory monocytes into TMEV-infected muscles leading to a predominance of relatively immature macrophages in SHP-1-deficient compared to WT muscle.

CD47 neutralization attenuates disease severity in wild type mice

SHP-1 controls macrophage activities including phagocytosis and cytokine production, particularly through the CD47-SIRPα-SHP-1 signaling axis following contact with $CD47^+$ targets (46, 51, 52). Additionally, CD47-integrin interactions control other important aspects of monocyte functions including transendothelial migration that might explain increased numbers of macrophages in me/me mouse muscle following TMEV infection (52–54). Therefore, we addressed whether muscle pathology in wild type mice could be ameliorated by blockade of CD47-SIRPα-SHP-1 signaling in macrophages. To do this, WT BL/6 mice were injected with a CD47-neutralizing antibody using an established protocol (55). As we had observed extensive TMEV infection of skeletal muscle at 5 days P.I., yet had not observed substantial calcification prior to 9 days P.I., we initiated injections of CD47-neutralizing antibody 5 days after infection. Mice were treated with anti-CD47 from days 5–13 days P.I. and were sacrificed at 16 days P.I. No differences in muscle pathology were observed between control groups (untreated or IgG-treated), therefore all control animals were pooled for quantification. Mice were assigned clinical disease scores daily from 9–16 days P.I. As expected, animals receiving anti-CD47 treatments exhibited a significant reduction in clinical disease scores compared to controls (Figure 5A). Upon dissection, mice receiving CD47-blocking antibody had reduced calcification of skeletal muscle compared to controls (Figure 5B). Quantification of alizarin red stainings demonstrated significantly decreased muscle calcification in anti-CD47-treated animals compared to controls, indicating that blocking CD47 attenuated muscle pathology (Figure 5C). These data suggest that antibody-mediated blockade of CD47 signaling to macrophages in wild type mice altered macrophage activity in ways that were protective against TMEV-induced muscle pathology as seen in SHP-$1^{-/-}$ mice.

Since the CD47 receptor, SIRPα, is predominantly expressed on macrophages (46, 51), macrophage phenotypic differences between control and anti-CD47-treated mice were analyzed. Indeed, upon immunofluorescence analysis of tissue sections, CD47-neutralized mice displayed elevated Ly6c and reduced F4/80 expression compared to controls (Figure 5D), correlating with the immature phenotype of macrophages observed in me/me muscle (Figure 4B–C). These data suggest that in SHP-$1^{-/-}$ mice, macrophage functions normally controlled by CD47-SIRPα-SHP-1 signaling inhibit extensive myofiber calcification and allow continued muscle function. Alternatively or additionally, expression of SHP-1 in wild type macrophages may promote macrophage differentiation in ways that are detrimental to muscle function.

Inflammatory M1 macrophages correlate with increased muscle pathology in wild type mice

As our data indicated that SHP-1 controlled TMEV-induced muscle pathology at the level of macrophages, we further analyzed an extended macrophage gene expression profile in these cells isolated from infected muscle. Thus, we used FACS to sort $CD45^{+}CD11b^{+}Ly6c^{+\,(hi\ and\ lo)}$ macrophages from skeletal muscle of me/me and WT mice at 5 days P.I. for subsequent RNA analysis. Interestingly, we observed significantly increased expression of various pro-inflammatory genes within sorted WT compared to me/me mouse macrophages (Figure 6A), including TNF-α, IL-1β, IL-6, Caspase 1, iNOS, IRF-1, IRF-5 and IRF-8. No significant differences in expression of M2-associated genes (Arginase 1, FIZZ1 or Ym1) were observed between WT and me/me macrophages (Figure 6A). These data demonstrated that while me/me mice display a much more pronounced infiltration of macrophages into infected muscle, me/me mouse macrophages were relatively immature compared to those in WT muscle, the latter maturing into classically activated (M1) macrophages. As no differences between M2-associated genes were observed between genotypes, these data support the idea that SHP-1 drives the maturation of muscle-infiltrating inflammatory monocytes into M1-like macrophages, likely contributing to inflammatory-mediated myofiber death and calcification.

Since the gene expression profile of wild type muscle-infiltrating macrophages corresponded with our previous observations of $SHP\text{-}1^{-/-}$ CNS-infiltrating macrophages (40, 41), we additionally sorted spinal cord-infiltrating $CD45^{hi}$ cells at 5 days P.I. in the same mice and analyzed an extended gene profile in these cells. CNS-infiltrating cells were gated on $CD45^{hi}$ as we have previously demonstrated that macrophages are the predominant CNS-infiltrating cells following TMEV infection (40, 41), Interestingly, although M1 genes were higher in wild type compared to me/me mouse muscle macrophages, these differences were either reversed or eliminated in CNS macrophages (Figure 6B), indicating that SHP-1 regulated macrophage maturation/differentiation within CNS tissue uniquely compared to that seen in skeletal muscle.

Depletion of macrophages reduces disease severity in wild type mice

As our data suggested that inflammatory M1-like macrophages contribute to muscle damage and calcification in wild type mice, we sought to determine if depletion of macrophages could inhibit muscle calcification in these animals. Clodronate liposomes have been extensively used to selectively deplete macrophages *in vivo* (56–58). Thus, wild type animals were injected with either control or clodronate liposomes every 3 days from 6 to 12 days P.I. and were sacrificed at 14 days P.I. Mice were assigned daily clinical disease scores from 8–14 days P.I. Animals receiving clodronate liposomes displayed significantly reduced clinical disease severity (Figure 7A), suggesting that depletion of macrophages reduced TMEV-induced muscle disease in wild type mice. Upon dissection, all five animals receiving control liposomes displayed moderate to severe signals of muscle calcification, while all 5 mice receiving clodronate liposomes were relatively free of muscle calcification (Figure 7B, left), signifying that depletion of macrophages restricts TMEV-induced muscle calcification in wild type mice. This was further demonstrated by closer inspection of the medial gastrocnemius muscle (zoomed image in Figure 7B, middle) and by alizarin red

staining (Figure 7B, right). Thus, these data confirmed that macrophages are the predominant cells contributing to TMEV-induced muscle calcification in wild type animals.

TMEV replicates to high levels in M1 macrophages of wild type mice

As we had seen increased maturation of classically activated macrophages in wild type compared to me/me muscle, it was of further interest to characterize the replicative capacity of TMEV in this population as it was reported that TMEV replicates in mature macrophages but not less mature lineage cells including monocytes (59–61). At 5 and 9 days post infection similar levels of TMEV antigen were found within myofibers between WT and SHP-$1^{-/-}$ mice (Figure 8A), indicating that TMEV infection of muscle occurred equally between these genotypes. Consistent with this observation, RNA analysis of whole skeletal muscle tissue confirmed similar levels of TMEV genomes between me/me and WT littermates at 5 days P.I., and between me^{v}/me^{v} and WT littermates at 9 days P.I. (Figure 8C). Nonetheless, immunofluorescent stainings showed that some $Ly6c^{+}$ cells were infected with TMEV (Figure 8B), and these appeared more prominent in muscle of wild type compared SHP-$1^{-/-}$ mice. To investigate this further, RNA analysis of muscle-infiltrating $CD45^{+}CD11b^{+}Ly6c^{+}$ macrophages revealed many more copies of TMEV genomes in muscle-infiltrating WT compared to me/me mouse macrophages (Figure 8C). These data demonstrated that although infection of muscle fibers appeared SHP-1-independent, TMEV preferentially replicated in WT compared to me/me mouse macrophages. In sum, SHP-1 drove both increased M1 differentiation and increased virus replication in macrophages, both of which were associated with increased inflammatory disease in skeletal muscle of wild type animals.

Discussion

The main phenotypic disease outcome following peripheral TMEV infection of suckling wild type mice is extensive calcification and immobilization of limb skeletal muscles. Further, mice deficient in SHP-1 on either of two different genetic backgrounds while displaying equal levels of infection of skeletal muscle compared to wild type animals, never displayed limb muscle calcification or immobilization. The present study was focused on understanding the basis for this dramatic phenotypic difference. First, we focused on the nature of ectopic calcification. In general, ectopic calcification is defined as an inappropriate mineralization of soft tissues and is divided into two classes: metastatic calcification occurs during a systemic mineral imbalance with elevated serum calcium and/or phosphorous levels; while dystrophic calcification occurs in the absence of a systemic mineral imbalance and results from tissue damage and cell death (62–64). Based on the observation that TMEV-induced calcification occurs within myofibers (Figure 2), the apparent fibrosis in skeletal muscle (Figures 1–2), the overwhelming tissue damage observed in infected muscles (Figures 1–2) and the resemblance of calcified myofibers with those from a murine model of Duchenne muscular dystrophy (*mdx* mice) (65, 66), we concluded that TMEV causes dystrophic calcification of degenerating myofibers in WT mice. Thus, there is likely to be a significant difference in either the production or removal of damaged myofibers that accounts for the high incidence of calcified fibers in wild type animals.

The finding that infection levels of muscle fibers were similar between genotypes (Figure 8), the entire lack of calcified myofibers in me/me mice and the observation that depletion of macrophages from wild type mice reduced muscle calcification supports the idea that an increased rate of myofiber cell death mediated by M1 macrophages in wild type compared to me/me mice is responsible for increased muscle disease in wild type animals. As such, SHP-1-mediated macrophage skewing toward an M1 phenotype in muscle may increase the expression of molecules detrimental to myofiber survival in virus-infected muscle as described in other disease models. For instance, many chronic inflammatory conditions resulting from tissue damage or infection are associated with cachexia, a process involving muscle wasting (67). Mounting evidence has implicated a major role of pro-inflammatory cytokines such as TNF-α, IL-1β and IL-6 in promoting muscle wasting (67, 68). In particular, TNF-α has been shown to reduce myotube protein content, induce muscle fiber decay, inhibit myogenic differentiation and trigger apoptosis of myofibers, while IL-1β has been reported to trigger iNOS-mediated muscle fiber necrosis (67, 69). Thus, it is a strong possibility that increased levels of pro-inflammatory cytokines secreted by M1 macrophages such as TNF-α, IL-1β and IL-6 in muscles from TMEV-infected WT mice may cause increased damage of myofibers or may disrupt muscle repair processes.

Our data suggests that the key immune regulator SHP-1 is a primary factor driving dystrophic calcification in wild type mice by promoting M1 maturation of inflammatory macrophages during TMEV infection of skeletal muscle. Beyond promoting an inflammatory M1 phenotype in wild type macrophages, TMEV also appeared to preferentially replicate in M1 macrophages in wild type skeletal muscle, compared to non-M1 macrophages in me/me mice (Figures 6 and 8). As such, TMEV may utilize various cellular pathways to its advantage in M1-differentiated macrophages as a strategy for maintaining infection in the face of an acute inflammatory response to the virus. The finding that TMEV replicates in terminally differentiated macrophages but not at earlier less-differentiated stages is consistent with previous studies including those with TMEV (59–61, 70–81). In accord with these observations and the finding that SHP-1 appeared to promote M1 differentiation, we propose that SHP-$1^{-/-}$ mouse macrophages are maintained at a less differentiated state of development within infected skeletal muscle and therefore do not provide suitable host factors for TMEV replication.

The data presented in this manuscript demonstrate unanticipated roles of SHP-1 in facilitating both the development of M1 macrophages and clinical tissue pathology following virus infection. At first sight this observation was surprising, as SHP-1 has been shown to limit M1 macrophage phenotype and extensive immune-mediated inflammatory tissue damage in the CNS (40, 41, 45). Consistent with this, production of inflammatory cytokines, proteolytic factors and nitric oxide by M1-like macrophages have been demonstrated to promote inflammatory demyelination (36). However, it has also been reported that SHP-1-deficient macrophages are defective in the ability to produce both IL-6 and IL-12 in response to TLR stimulation, indicating that SHP-1 is a positive regulator of these M1 responses (82). Thus, the function of SHP-1 in macrophages may be context-specific in which tissue factors play a deciding role on M1-skewing of macrophages and M1-mediated tissue damage. Therefore, the mechanisms by which tissue and pathogen-associated factors may influence the role of SHP-1 in macrophage differentiation need to be

further clarified. We are currently focused on deciphering these factors in skeletal muscle and CNS tissue in which TMEV infection produces an entirely different pattern of macrophage differentiation and tissue damage in wild type and me/me mice. Together, these data suggest that SHP-1 governs macrophage maturation in unique ways dependent on the tissue type, and a common denominator coming from our studies is that TMEV replication and TMEV-induced tissue pathology occurs primarily via M1 macrophages.

Arboviruses including flaviruses and alphaviruses are emerging global disease threats that are often associated with muscle and/or CNS manifestations (1, 21). Furthermore, arbovirus infections associated with skeletal muscle involvement and often subsequent neurological complications pose a particularly escalating threat in children (32–35). Myositis disorders in humans are thought to be multifactorial diseases involving genetic factors and environmental triggers such as virus infections, yet these disorders remain poorly characterized with few treatment options available (83–88). Thus, there is an urgent need to define better animal models to study virus-induced myositis. As flaviviruses, alphaviruses and picornaviruses including TMEV possess positive-sensed single-stranded RNA genomes, this report describes a relevant model system to investigate key immune regulators, including SHP-1, in virus-induced myositis in young animals.

As depicted in Figure 9, we predict that following TMEV infection of muscle inflammatory monocytes are recruited to the site of infection in WT and SHP-1-deficient mice, where these monocytes mature into M1 macrophages in WT animals. As it has been established that TMEV can infect immature monocyte-like cells yet only replicate in mature macrophages (59–61), we predict that these mature M1-like macrophages provide a substrate for TMEV replication and additionally contribute to myofiber damage likely via proinflammatory factors (red lightening bolt). Additionally, active TMEV replication in macrophages has been shown to trigger macrophage apoptosis (60, 61, 89–91), likely contributing to decreased numbers of macrophages in WT compared to me/me muscle. Alternatively, in the absence of SHP-1, muscle-infiltrating monocytes do not mature properly, maintaining a persistent rather than abortive infection of TMEV in these cells, likely contributing to the increased numbers of cells observed in SHP-$1^{-/-}$ muscle compared to WT. Overall, the primary difference seen between WT and SHP-1-deficient animals is the observation of myofiber death/calcification in wild type but not SHP-1-deficient mice, and depletion of macrophages in TMEV-infected wild type mice was shown to inhibit muscle calcification. Thus, our data suggest that following TMEV infection of muscle, SHP-1 promotes M1 maturation of macrophages, facilitating myofiber damage and subsequent disease pathology; whereas immature SHP-1-deficient macrophages do not contribute to muscle damage and may additionally benefit muscle in some way, avoiding clinical muscle pathology.

Acknowledgements

We thank Howard L. Lipton from the University of Illinois at Chicago for the generous donation of rabbit anti-BeAn TMEV antisera for immunofluorescence analyses. We would additionally like to thank Karen Gentile and Frank Middleton at the SUNY Upstate Microarray core for their assistance in RNA extraction and analysis via the QuantiGene Plex 2.0 Assay.

This research was supported by the National Institute of Health (NIH) grant R01 NS072051.

References

1. Crum-Cianflone NF. Bacterial, fungal, parasitic, and viral myositis. Clin. Microbiol. Rev. 2008; 21:473–494. [PubMed: 18625683]
2. Josselson J, Pula T, Sadler JH. Acute rhabdomyolysis associated with an echovirus 9 infection. Arch. Intern. Med. 1980; 140:1671–1672. [PubMed: 7458499]
3. Jehn UW, Fink MK. Myositis, myoglobinemia, and myoglobinuria associated with enterovirus echo 9 infection. Arch. Neurol-Chicago. 1980; 37:457–458. [PubMed: 7387495]
4. Dunnet J, Paton JY, Robertson CE. Acute renal failure and Coxsackie viral infection. Clin. Nephrol. 1981; 16:262–326. [PubMed: 7307354]
5. Chariot P, Ruet E, Authier FJ, Levy Y, Gherardi R. Acute rhabdomyolysis in patients infected by human immunodeficiency virus. Neurology. 1994; 44:1692–1696. [PubMed: 7936298]
6. Dalakas MC, Pezeshkpour GH, Gravell M, Sever JL. Polymyositis associated with AIDS retrovirus. J. Amer. Med. Assoc. 1986; 256:2381–2383.
7. Leon-Monzon M, Illa I, Dalakas MC. Polymyositis in patients infected with human T-cell leukemia virus type I: the role of the virus in the cause of the disease. Ann. Neurol. 1994; 36:643–649. [PubMed: 7944297]
8. Morgan OS, Rodgers-Johnson P, Mora C, Char G. HTLV-1 and polymyositis in Jamaica. Lancet. 1989; 2:1184–1187. [PubMed: 2572904]
9. Nishikai M, Sato A. Human T lymphotropic virus type I and polymyositis and dermatomyositis in Japan. Arthritis Rheum. 1991; 34:791–792. [PubMed: 2053931]
10. Di Muzio A, Bonetti B, Capasso M, Panzeri L, Pizzigallo E, Rizzuto N, Uncini A. Hepatitis C virus infection and myositis: a virus localization study. Neuromuscular Disord. 2003; 13:68–71.
11. Mihas AA, Kirby JD, Kent SP. Hepatitis B antigen and polymyositis. J. Amer. Med. Assoc. 1978; 239:221–222.
12. Nojima T, Hirakata M, Sato S, Fujii T, Suwa A, Mimori T, Ikeda Y. A case of polymyositis associated with hepatitis B infection. Clin. Exp. Rheumatol. 2000; 18:86–88. [PubMed: 10728451]
13. Chopy D, Detje CN, Lafage M, Kalinke U, Lafon M. The type I interferon response bridles rabies virus infection and reduces pathogenicity. J. Neurovirol. 2011; 17:353–367. [PubMed: 21805057]
14. Tsiang H. Rabies virus infection of myotubes and neurons as elements of the neuromuscular junction. Rev. Infect. Dis. 1988; 4(10 Suppl):S733–S738. [PubMed: 3060959]
15. Park CH, Kondo M, Inoue S, Noguchi A, Oyamada T, Yoshikawa H, Yamada A. The histopathogenesis of paralytic rabies in six-week-old C57BL/6J mice following inoculation of the CVS-11 strain into the right triceps surae muscle. J. Vet. Med. Sci. 2006; 68:589–595. [PubMed: 16820716]
16. Bachis A, Aden SA, Nosheny RL, Andrews PM, Mocchetti I. Axonal transport of human immunodeficiency virus type 1 envelope protein glycoprotein 120 is found in association with neuronal apoptosis. J. Neurosci. 2006; 26:6771–6780. [PubMed: 16793884]
17. Shindler KS, Chatterjee D, Biswas K, Goyal A, Dutt M, Nassrallah M, Khan RS, Das Sarma K. Macrophage-mediated optic neuritis induced by retrograde axonal transport of spike gene recombinant mouse hepatitis virus. J. Neuropath. Exp. Neur. 2011; 70:470–480. [PubMed: 21572336]
18. Ahmed F, MacArthur L, De Bernardi MA, Mocchetti I. Retrograde and anterograde transport of HIV protein gp120 in the nervous system. Brain Behav. Immun. 2009; 23:355–364. [PubMed: 19111924]
19. Mori I, Kimura Y. Neuropathogenesis of influenza virus infection in mice. Microbes Infect. 2001; 3:475–479. [PubMed: 11377209]
20. Das Sarma J, Kenyon LC, Hingley ST, Shindler KS. Mechanisms of primary axonal damage in a viral model of multiple sclerosis. J. Neurosci. 2009; 29:10272–10280. [PubMed: 19692601]
21. West Nile virus and other arboviral diseases--United States. Morbidity and mortality weekly report. 2013; 62:513–517. [PubMed: 23803959]

22. Lidbury BA, Simeonovic C, Maxwell GE, Marshall ID, Hape AJ. Macrophage-induced muscle pathology results in morbidity and mortality for Ross River virus-infected mice. J. Infect Dis. 2000; 181:27–34. [PubMed: 10608747]
23. Herrero LJ, Nelson M, Srikiatkhachorn A, Gu R, Anantapreecha S, Fingerle-Rowson G, Bucala R, Morand E, Santos LL, Mahalingam S. Critical role for macrophage migration inhibitory factor (MIF) in Ross River virus-induced arthritis and myositis. Proc. Natl. Acad. Sci. USA. 2011; 108:12048–12053. [PubMed: 21730129]
24. Morrison TE, Whitmore AC, Shabman RS, Lidbury BA, Mahalingam S, Heise MT. Characterization of Ross River virus tropism and virus-induced inflammation in a mouse model of viral arthritis and myositis. J. Virol. 2006; 80:737–749. [PubMed: 16378976]
25. Harley D, Bossingham D, Purdie DM, Pandeya N, Sleigh AC. Ross River virus disease in tropical Queensland: evolution of rheumatic manifestations in an inception cohort followed for six months. Med. J. Australia. 2002; 177:352–355. [PubMed: 12358576]
26. Seay AR, Wolinsky JS. Ross River virus-induced demyelination: I. Pathogenesis and histopathology. Ann. Neurol. 1982; 12:380–389. [PubMed: 6293370]
27. Sane J, Kurkela S, Desdouits M, Kalimo H, Mazalrey S, Lokki ML, Vaheri A, Helve T, Tornwall J, Huerre M, Butler-Browne G, Ceccaldi PE, Gessain A, Vapalahti O. Prolonged myalgia in Sindbis virus infection: case description and in vitro infection of myotubes and myoblasts. J. Infect. Dis. 2012; 206:407–414. [PubMed: 22615321]
28. Kurkela S, Manni T, Myllynen J, Vaheri A, Vapalahti O. Clinical and laboratory manifestations of Sindbis virus infection: prospective study, Finland, 2002–2003. J. Infect. Dis. 2005; 191:1820–1829. [PubMed: 15871114]
29. Assuncao-Miranda I, Cruz-Oliveira C, Da Poian AT. Molecular mechanisms involved in the pathogenesis of alphavirus-induced arthritis. Biomed Res. Int. 2013
30. Couderc T, Chretien F, Schilte C, Disson O, Brigitte M, Guivel-Benhassine F, Touret Y, Barau G, Cayet N, Schuffenecker I, Despres P, Arenzana-Seisdedos F, Michault A, Albert ML, Lecuit M. A mouse model for Chikungunya: young age and inefficient type-I interferon signaling are risk factors for severe disease. PLoS Pathog. 2008; 4:e29. [PubMed: 18282093]
31. Rohatgi A, Corbo JC, Monte K, Higgs S, Vanlandingham DL, Kardon G, Lenschow DJ. Infection of myofibers contributes to increased pathogenicity during infection with an epidemic strain of chikungunya virus. J. Virol. 2014; 88:2414–2425. [PubMed: 24335291]
32. Carod-Artal FJ, Wichmann O, Farrar J, Gascon J. Neurological complications of dengue virus infection. Lancet Neurol. 2013; 12:906–919. [PubMed: 23948177]
33. Rajajee S, Ezhilarasi S, Rajarajan K. Benign acute childhood myositis. Indian J. Pediatr. 2005; 72:399–400. [PubMed: 15973022]
34. Finsterer J, Kongchan K. Severe, persisting, steroid-responsive Dengue myositis. J. Clin. Virol. 2006; 35:426–428. [PubMed: 16414305]
35. Paliwal VK, Garg RK, Juyal R, Husain N, Verma R, Sharma PK, Singh MK. Acute dengue virus myositis: a report of seven patients of varying clinical severity including two cases with severe fulminant myositis. J. Neurol. Sci. 2011; 300:14–18. [PubMed: 21081241]
36. Oleszak EL, Chang JR, Friedman H, Katsetos CD, Platsoucas CD. Theiler's virus infection: a model for multiple sclerosis. Clin. Microbiol. Rev. 2004; 17:174–207. [PubMed: 14726460]
37. Rustigian R, Pappenheimer AM, Le BT. The resistance of mice to myositis and central nervous system infection following immunization with DGVII mouse encephalomyelitis virus. J. Immunol. 1951; 67:225–234. [PubMed: 14888886]
38. Rustigian R, Pappenheimer AM. Myositis in mice following intramuscular injection of viruses of the mouse encephalomyelitis group and of certain other neurotropic viruses. J. Exp. Med. 1949; 89:69–92. [PubMed: 18099166]
39. Gomez RM, Rinehart JE, Wollmann R, Roos RP. Theiler's murine encephalomyelitis virus-induced cardiac and skeletal muscle disease. J. Virol. 1996; 70:8926–8933. [PubMed: 8971022]
40. Christophi GP, Massa PT. Central neuroinvasion and demyelination by inflammatory macrophages after peripheral virus infection is controlled by SHP-1. Viral Immunol. 2009; 22:371–387. [PubMed: 19951174]

41. Christophi GP, Hudson CA, Panos M, Gruber RC, Massa PT. Modulation of macrophage infiltration and inflammatory activity by the phosphatase SHP-1 in virus-induced demyelinating disease. J. Virol. 2009; 83:522–539. [PubMed: 18987138]
42. Massa PT, Ropka SL, Saha S, Fecenko KL, Beuler KL. Critical role for protein tyrosine phosphatase SHP-1 in controlling infection of central nervous system glia and demyelination by Theiler's murine encephalomyelitis virus. J. Virol. 2002; 76:8335–8346. [PubMed: 12134038]
43. Chong ZZ, Maiese K. The Src homology 2 domain tyrosine phosphatases SHP-1 and SHP-2: diversified control of cell growth, inflammation, and injury. Histol. Histopathol. 2007; 22:1251–1267. [PubMed: 17647198]
44. Zhang J, Somani AK, Siminovitch KA. Roles of the SHP-1 tyrosine phosphatase in the negative regulation of cell signalling. Semin. Immunol. 2000; 12:361–378. [PubMed: 10995583]
45. Croker BA, Lawson BR, Rutschmann S, Berger M, Eidenschenk C, Blasius AL, Moresco EM, Sovath S, Cengia L, Shultz LD, Theofilopoulos AN, Pettersson S, Beutler BA. Inflammation and autoimmunity caused by a SHP1 mutation depend on IL-1, MyD88, and a microbial trigger. Proc. Natl Acad. Sci. USA. 2008; 105:15028–15033. [PubMed: 18806225]
46. Okazawa H, Motegi S, Ohyama N, Ohnishi H, Tomizawa T, Kaneko Y, Oldenborg PA, Ishikawa O, Matozaki T. Negative regulation of phagocytosis in macrophages by the CD47-SHPS-1 system. J. Immunol. 2005; 174:2004–2011. [PubMed: 15699129]
47. Murray PJ, Wynn TA. Protective and pathogenic functions of macrophage subsets. Nat. Rev. Immunol. 2011; 11:723–737. [PubMed: 21997792]
48. Crane MJ, Daley JM, van Houtte O, Brancato SK, Henry WL Jr, Albina JE. The monocyte to macrophage transition in the murine sterile wound. PloS ONE. 2014; 9:e86660. [PubMed: 24466192]
49. Arnold L, Henry A, Poron F, Baba-Amer Y, van Rooijen N, Plonquet A, Gherardi RK, Chazaud B. Inflammatory monocytes recruited after skeletal muscle injury switch into antiinflammatory macrophages to support myogenesis. J. Exp. Med. 2007; 204:1057–1069. [PubMed: 17485518]
50. Gordon S, Taylor PR. Monocyte and macrophage heterogeneity. Nat. Rev. Immunol. 2005; 5:953–964. [PubMed: 16322748]
51. Matozaki T, Murata Y, Okazawa H, Ohnishi H. Functions and molecular mechanisms of the CD47-SIRPalpha signalling pathway. Trends Cell Biol. 2009; 19:72–80. [PubMed: 19144521]
52. Oldenborg PA. CD47: A Cell Surface Glycoprotein Which Regulates Multiple Functions of Hematopoietic Cells in Health and Disease. ISRN Hematology. 2013:614619. [PubMed: 23401787]
53. Toledano N, Gur-Wahnon D, Ben-Yehuda A, Rachmilewitz J. Novel CD47: SIRPalpha dependent mechanism for the activation of STAT3 in antigen-presenting cell. PloS ONE. 2013; 8:e75595. [PubMed: 24073274]
54. Azcutia V, Stefanidakis M, Tsuboi N, Mayadas T, Croce KJ, Fukuda D, Aikawa M, Newton G, Luscinskas FW. Endothelial CD47 promotes vascular endothelial-cadherin tyrosine phosphorylation and participates in T cell recruitment at sites of inflammation in vivo. J. Immunol. 2012; 189:2553–2562. [PubMed: 22815286]
55. Han MH, Lundgren DH, Jaiswal S, Chao M, Graham KL, Garris CS, Axtell RC, Ho PP, Lock CB, Woodard JI, Brownell SE, Zoudilova M, Hunt JF, Baranzini SE, Butcher EC, Raine CS, Sobel RA, Han DK, Weissman I, Steinman L. Janus-like opposing roles of CD47 in autoimmune brain inflammation in humans and mice. J. Exp. Med. 2012; 209:1325–1334. [PubMed: 22734047]
56. Van Rooijen N, Sanders A. Liposome mediated depletion of macrophages: mechanism of action, preparation of liposomes and applications. J. Immunol. Methods. 1994; 174:83–93. [PubMed: 8083541]
57. Ramachandran P, Pellicoro A, Vernon MA, Boulter L, Aucott RL, Ali A, Hartland SN, Snowdon VK, Cappon A, Gordon-Walker TT, Williams MJ, Dunbar DR, Manning JR, van Rooijen N, Fallowfield JA, Forbes SJ, Iredale JP. Differential Ly-6C expression identifies the recruited macrophage phenotype, which orchestrates the regression of murine liver fibrosis. Proc. Natl Acad Sci. USA. 2012; 109:E3186–E3195. [PubMed: 23100531]

58. Villalta SA, Rinaldi C, Deng B, Liu G, Fedor B, Tidball JG. Interleukin-10 reduces the pathology of mdx muscular dystrophy by deactivating M1 macrophages and modulating macrophage phenotype. Hum. Mol. Genet. 2011; 20:790–805. [PubMed: 21118895]
59. Jelachich ML, Bandyopadhyay P, Blum K, Lipton HL. Theiler's virus growth in murine macrophage cell lines depends on the state of differentiation. Virology. 1995; 209:437–444. [PubMed: 7778279]
60. Jelachich ML, Reddi HV, Trottier MD, Schlitt BP, Lipton HL. Susceptibility of peritoneal macrophages to infection by Theiler's virus. Virus Res. 2004; 104:123–127. [PubMed: 15246649]
61. Jelachich ML, Bramlage C, Lipton HL. Differentiation of M1 myeloid precursor cells into macrophages results in binding and infection by Theiler's murine encephalomyelitis virus and apoptosis. J. Virol. 1999; 73:3227–3235. [PubMed: 10074176]
62. Li Q, Uitto J. Mineralization/anti-mineralization networks in the skin and vascular connective tissues. Am. J. Pathol. 2013; 183:10–18. [PubMed: 23665350]
63. Leone A, Costantini AM, Brigida R, Antoniol OM, Antonelli-Incalzi R, Bonomo L. Soft-tissue mineralization in Werner syndrome. Skeletal Radiol. 2005; 34:47–51. [PubMed: 15138723]
64. Giachelli CM. Ectopic calcification: gathering hard facts about soft tissue mineralization. Am. J. Pathol. 1999; 154:671–675. [PubMed: 10079244]
65. Mizunoya W, Upadhaya R, Burczynski FJ, Wang G, Anderson JE. Nitric oxide donors improve prednisone effects on muscular dystrophy in the mdx mouse diaphragm. Am. J. Physiol-Cell Ph. 2011; 300:C1065–C1077.
66. Verma M, Asakura Y, Hirai H, Watanabe S, Tastad C, Fong GH, Ema M, Call JA, Lowe DA, Asakura A. Flt-1 haploinsufficiency ameliorates muscular dystrophy phenotype by developmentally increased vasculature in mdx mice. Hum. Mol. Genet. 2010; 19:4145–4159. [PubMed: 20705734]
67. Pajak B, Orzechowska S, Pijet B, Pijet M, Pogorzelska A, Gajkowska B, Orzechowski A. Crossroads of cytokine signaling--the chase to stop muscle cachexia. J. Physiol. Pharmacol. 2008; 9(59 Suppl):251–264. [PubMed: 19261984]
68. Sharma R, Anker SD. Cytokines, apoptosis and cachexia: the potential for TNF antagonism. Int. J. Cardiol. 2002; 85:161–171. [PubMed: 12163221]
69. Schmidt J, Barthel K, Zschuntzsch J, Muth IE, Swindle EJ, Hombach A, Sehmisch S, Wrede A, Luhder F, Gold R, Dalakas MC. Nitric oxide stress in sporadic inclusion body myositis muscle fibres: inhibition of inducible nitric oxide synthase prevents interleukin-1beta-induced accumulation of beta-amyloid and cell death. Brain. 2012; 135:1102–1114. [PubMed: 22436237]
70. Chattergoon MA, Latanich R, Quinn J, Winter ME, Buckheit RW 3rd, Blankson JN, Pardoll D, Cox AL. HIV and HCV activate the inflammasome in monocytes and macrophages via endosomal Toll-like receptors without induction of type 1 interferon. PLoS Pathog. 2014; 10:e1004082. [PubMed: 24788318]
71. Guo H, Gao J, Taxman DJ, Ting JP, Su L. HIV-1 Infection Induces IL-1beta Production via TLR8-Dependent and NLRP3-Inflammasome Mechanisms in Human Monocytes. J. Biol. Chem. 2014; 289:21716–21726. [PubMed: 24939850]
72. Schlaepfer E, Rochat MA, Duo L, Speck RF. Triggering TLR2, 3, 4, 5 and 8 reinforces the restrictive nature of M1- and M2-polarized macrophages to HIV. J. Virol. 2014; 88:9769–9781. [PubMed: 24942590]
73. Herbein G, Varin A. The macrophage in HIV-1 infection: from activation to deactivation? Retrovirology. 2010; 7:33. [PubMed: 20380696]
74. Alhoot MA, Wang SM, Sekaran SD. Inhibition of dengue virus entry and multiplication into monocytes using RNA interference. PLoS Negl Trop. Dis. 2011; 5:e1410. [PubMed: 22140591]
75. Halstead SB. Antibody, macrophages, dengue virus infection, shock, and hemorrhage: a pathogenetic cascade. Rev. Infect. Dis. 1989; 4(11 Suppl):S830–S839. [PubMed: 2665015]
76. O'Sullivan MA, Killen HM. The differentiation state of monocytic cells affects their susceptibility to infection and the effects of infection by dengue virus. J. Gen. Virol. 1994; 75(Pt 9):2387–2392. [PubMed: 8077937]

77. Chen YC, Wang SY, King CC. Bacterial lipopolysaccharide inhibits dengue virus infection of primary human monocytes/macrophages by blockade of virus entry via a CD14-dependent mechanism. J. Virol. 1999; 73:2650–2657. [PubMed: 10074110]
78. Ahmed S, Arif F, Yahya Y, Rehman A, Abbas K, Ashraf S, Akram DS. Dengue fever outbreak in Karachi 2006--a study of profile and outcome of children under 15 years of age. J. Pak. Med. Assoc. 2008; 58:4–8. [PubMed: 18297966]
79. Pham AM, Langlois RA, TenOever BR. Replication in cells of hematopoietic origin is necessary for Dengue virus dissemination. PLoS Pathog. 2012; 8:e1002465. [PubMed: 22241991]
80. Perry ST, Buck MD, Lada SM, Schindler C, Shresta S. STAT2 mediates innate immunity to Dengue virus in the absence of STAT1 via the type I interferon receptor. PLoS Pathog. 2011; 7:e1001297. [PubMed: 21379341]
81. Sun P, Kochel TJ. The battle between infection and host immune responses of dengue virus and its implication in dengue disease pathogenesis. Sci. World J. 2013
82. Zhou D, Collins CA, Wu P, Brown EJ. Protein tyrosine phosphatase SHP-1 positively regulates TLR-induced IL-12p40 production in macrophages through inhibition of phosphatidylinositol 3-kinase. J. Leukocyte Biol. 2010; 87:845–855. [PubMed: 20145200]
83. Rayavarapu S, Coley W, Kinder TB, Nagaraju K. Idiopathic inflammatory myopathies: pathogenic mechanisms of muscle weakness. Skeletal muscle. 2013; 3:13. [PubMed: 23758833]
84. Stoermer KA, Burrack A, Oko L, Montgomery SA, Borst LB, Gill RG, Morrison TE. Genetic ablation of arginase 1 in macrophages and neutrophils enhances clearance of an arthritogenic alphavirus. J. Immunol. 2012; 189:4047–4059. [PubMed: 22972923]
85. Uchiyama T, Arai K, Yamamoto-Tabata T, Hirai K, Kishimoto K, Nakamura Y, Hattori T. Generalized myositis mimicking polymyositis associated with chronic active Epstein-Barr virus infection. J. Neurol. 2005; 252:519–525. [PubMed: 15742118]
86. Rothwell S, Cooper RG, Lamb JA, Chinoy H. Entering a new phase of immunogenetics in the idiopathic inflammatory myopathies. Curr. Opin. Rheumatol. 2013; 25:735–741. [PubMed: 24067379]
87. Lazarou IN, Guerne PA. Classification, diagnosis, and management of idiopathic inflammatory myopathies. J. Rheumatol. 2013; 40:550–564. [PubMed: 23504386]
88. Gan L, Miller FL. State of the art: what we know about infectious agents and myositis. Curr. Opin. Rheumatol. 2011; 23:585–594. [PubMed: 21885972]
89. Son KN, Liang Z, Lipton HL. Mutation of the Theiler's virus leader protein zinc-finger domain impairs apoptotic activity in murine macrophages. Virus research. 2013; 177:222–225. [PubMed: 24036175]
90. Jelachich ML, Lipton HL. Restricted Theiler's murine encephalomyelitis virus infection in murine macrophages induces apoptosis. J. Gen. Virol. 1999; 80(Pt 7):1701–1705. [PubMed: 10423138]
91. Jelachich ML, Lipton HL. Theiler's murine encephalomyelitis virus induces apoptosis in gamma interferon-activated M1 differentiated myelomonocytic cells through a mechanism involving tumor necrosis factor alpha (TNF-alpha) and TNF-alpha-related apoptosis-inducing ligand. J. Virol. 2001; 75:5930–5938. [PubMed: 11390594]

Glossary

BL/6	C57BL/6J
C3H	C3HeB/FeJLe
CD11b	cluster of differentiation molecule 11b
CD45	leukocyte common antigen CD47, cluster of differentiation 47
FSC	forward scatter
iNOS	inducible nitric oxide synthase

Ly6c	lymphocyte antigen 6c
M1	type 1 macrophage
M2	type 2 macrophage me, motheaten
me^{v}	viable motheaten
P.I.	post infection
SHP-1	src homology region 2 domain-containing phosphatase 1
SIRPα	signal regulatory protein alpha
SSC	side scatter
TMEV	Theiler's murine encephalomyelitis virus

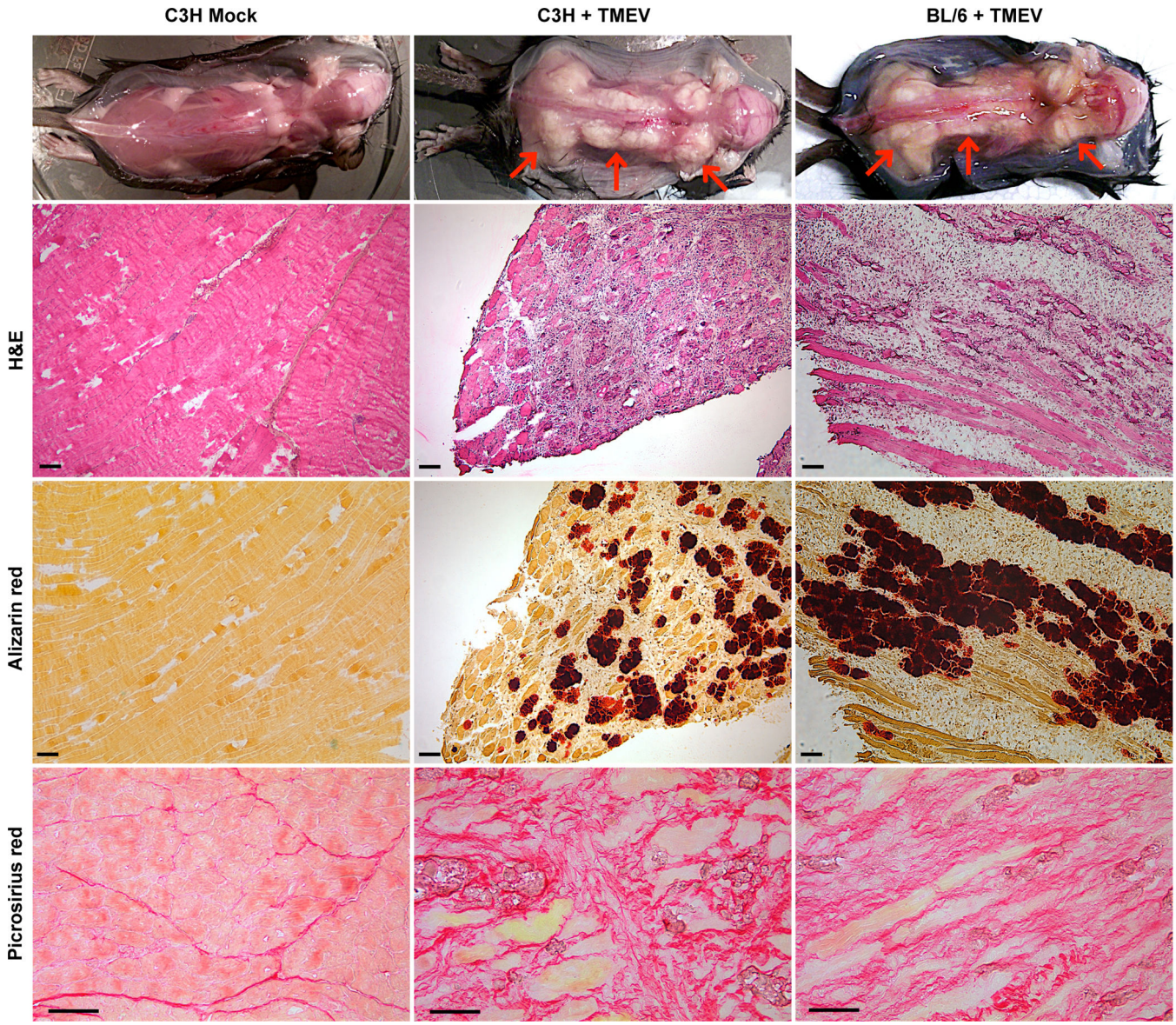

Figure 1. TMEV-induced muscle pathology in WT mice

12 day old wild type C3H or C57BL/6 mice were inoculated IP with 6×10^6 PFU TMEV or mock supernatant (C3H only) and sacrificed at 14–15 days P.I. Top: representative images of observed skeletal muscle disease upon dissection; red arrows indicate calcified (white) muscle. Middle two rows: serial muscle sections stained with H&E or Alizarin red S; scale bars represent 200μm, n=4. Bottom row: muscle sections were stained with picrosirius red; scale bars depict 50μm, n=4.

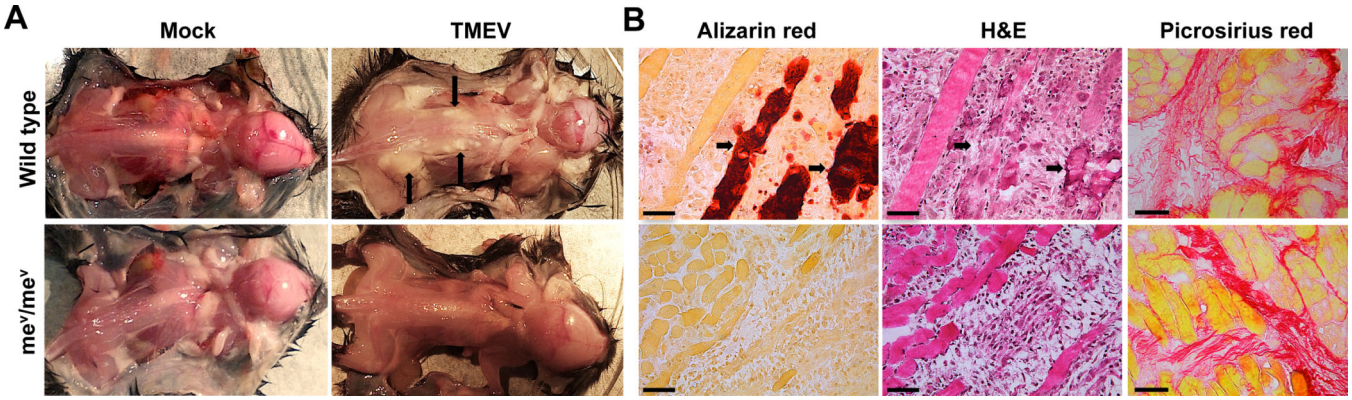

Figure 2. Muscle pathology in WT and SHP-1$^{-/-}$ mice

12 day old me^{v}/me^{v} mice (bottom) and WT littermates (top) were infected with 6×10^{5} PFU TMEV or mock supernatant and sacrificed at 9 days P.I. (A) Representative images of dissected mice; arrows indicate observed muscle disease by apparent calcification. (B) Alizarin red (left) and H&E (middle) stains were performed on serial skeletal muscle sections; arrows point to corresponding calcified fibers in adjacent sections. Scale bars represent 50μm, n=3. (B, right) Muscle sections were stained with picrosirius red, n=4, scale bars depict 50μm.

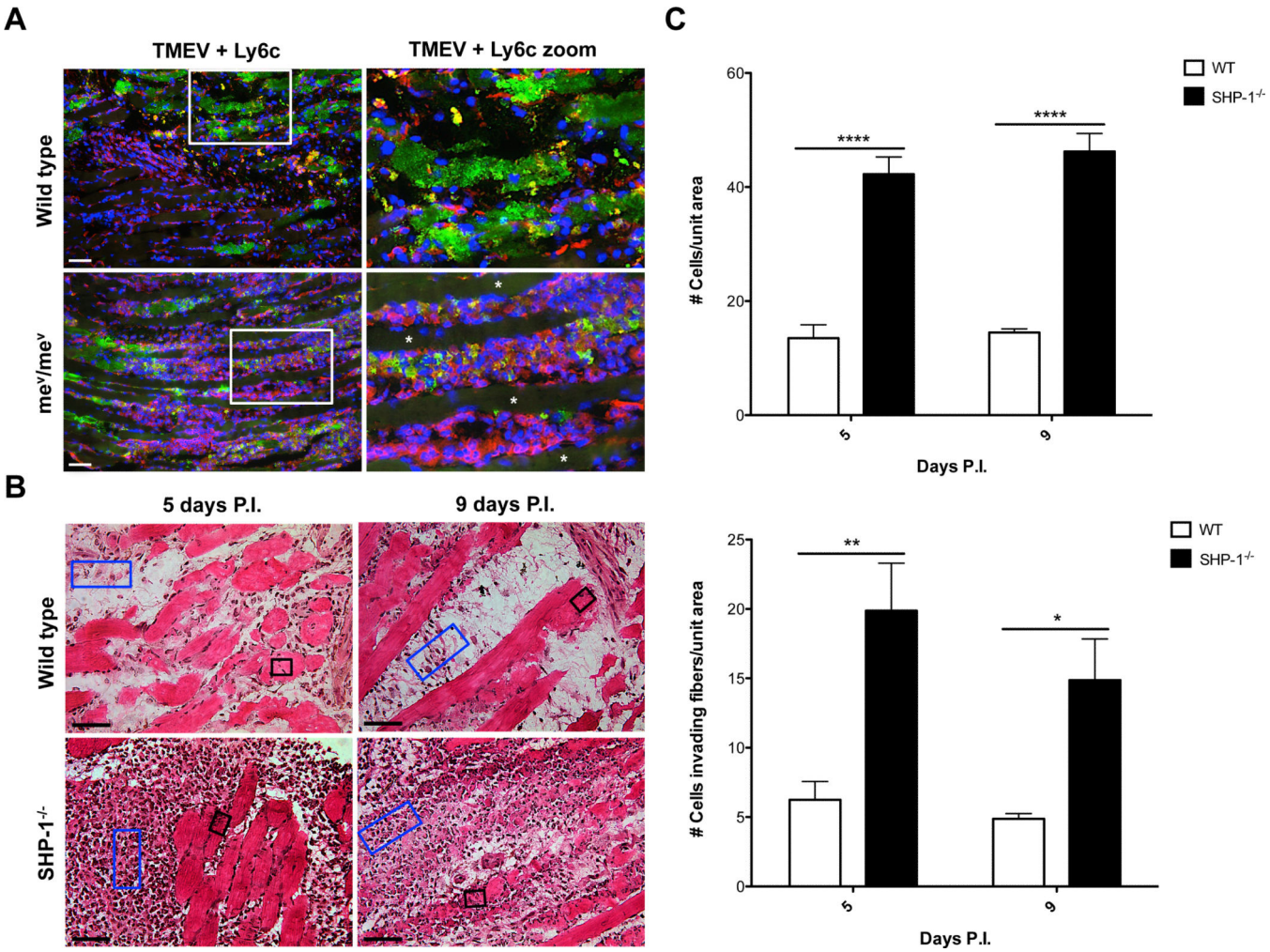

Figure 3. Infiltration of WT and SHP-1$^{-/-}$ cells into skeletal muscle following infection

(A) me^{v}/me^{v} mice and WT littermates were sacrificed at 9 days P.I. and muscle sections were labeled with antibodies against Ly6c (red), TMEV (green) and stained with DAPI (blue); asterisks illustrate uninfected myofibers. Scale bars depict 100μm, n=3. (B) me/me mice and WT littermates (n=2) and me^{v}/me^{v} mice and WT littermates (n=2) were sacrificed at 5 days P.I., and me^{v}/me^{v} mice and WT littermates (n=4) were sacrificed at 9 days P.I. Cell counts were performed on H&E stained muscle sections to determine the average number of cells per unit area within lesions (blue rectangles) or within intact myofibers (black boxes). Representative images of me/me and WT littermates at 5 days P.I. and me^{v}/me^{v} and WT littermates at 9 days P.I. shown; scale bars depict 50μm. (C) Graphical representation portraying the average number of cells per unit area with lesions (top) and average number of cells invading fibers per unit area (bottom).

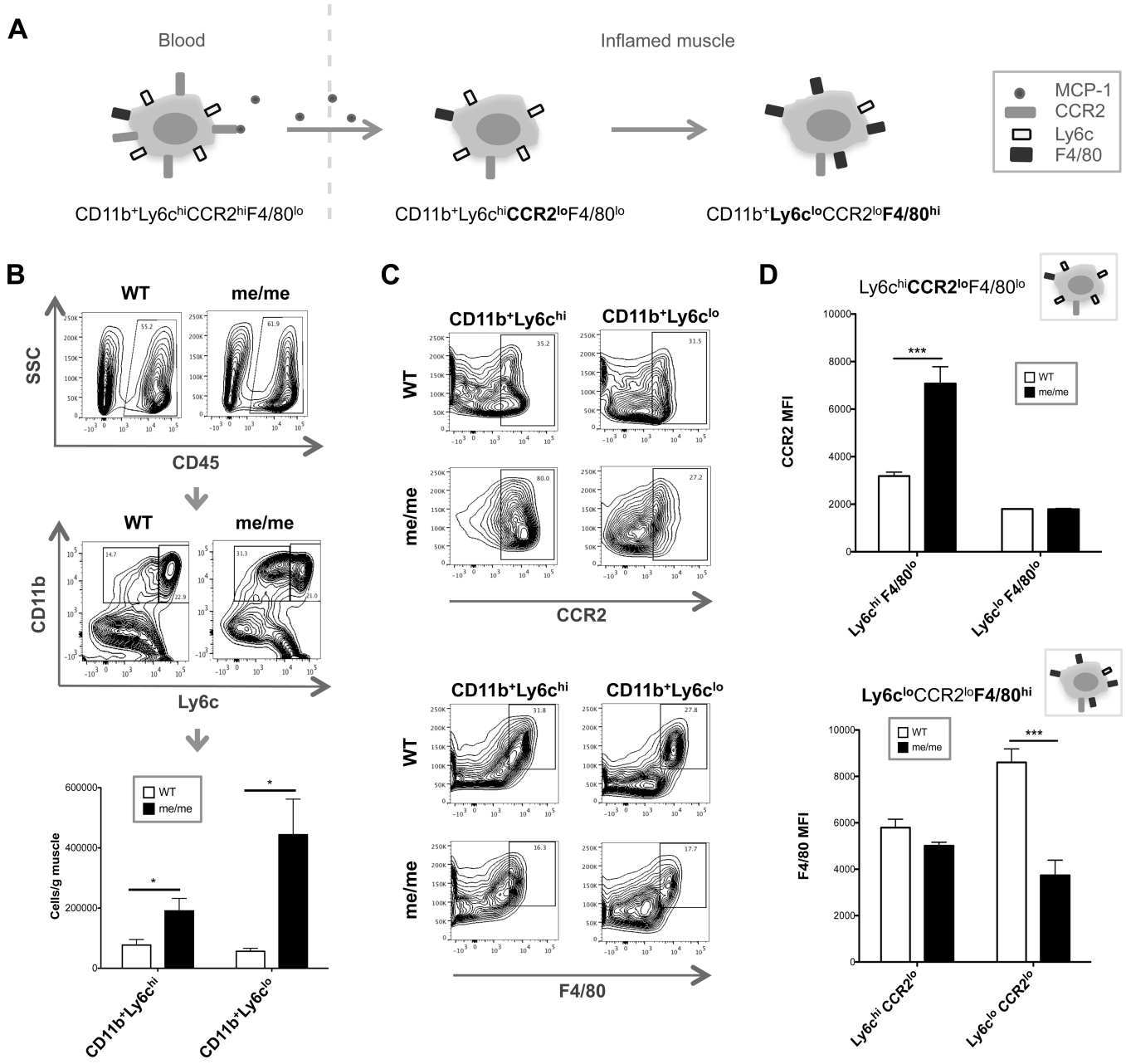

Figure 4. Quantification and phenotypic analysis of muscle-infiltrating monocytes

(A) Cartoon schematic depicting typical maturation of blood-born inflammatory monocytes into macrophages in inflamed tissues, demonstrating downregulation of CCR2 followed by downregulation of Ly6c and upregulation of F4/80. (B–D) WT and me/me mice were sacrificed at 5 days P.I. and cells were isolated from skeletal muscle for flow cytometry analysis. (B) Representative gating strategy of WT and me/me muscle depicting initial $CD45^+$ gate (top) to exclude myofiber debris and non-hematopoietic cells, and $CD11b^+Ly6c^{hi}$ (right) or $CD11b^+Ly6c^{lo}$ (left) monocyte gates (middle panel). Bottom graph displays absolute numbers of $CD11b^+Ly6c^{hi}$ or $CD11b^+Ly6c^{lo}$ cells per gram of skeletal muscle quantified; n=3, performed in triplicate. (C–D) F4/80 and CCR2 expression was

evaluated in $CD45^+CD11b^+Ly6c^{lo}$ and $CD45^+CD11b^+Ly6c^{hi}$ cells. (C) Representative contour plots shown of WT (top) and me/me (bottom) mice. F4/80 gate depicts $F4/80^{hi}$ cells, while CCR2 gate depicts $CCR2^+$ cells. (D) CCR2 (top) or F4/80 (bottom) MFI levels were quantified from $F4/80^{lo}$ or $CCR2^{lo}$ populations, respectively, with corresponding maturation stage cartoons as described in (A). N=3, performed in duplicate.

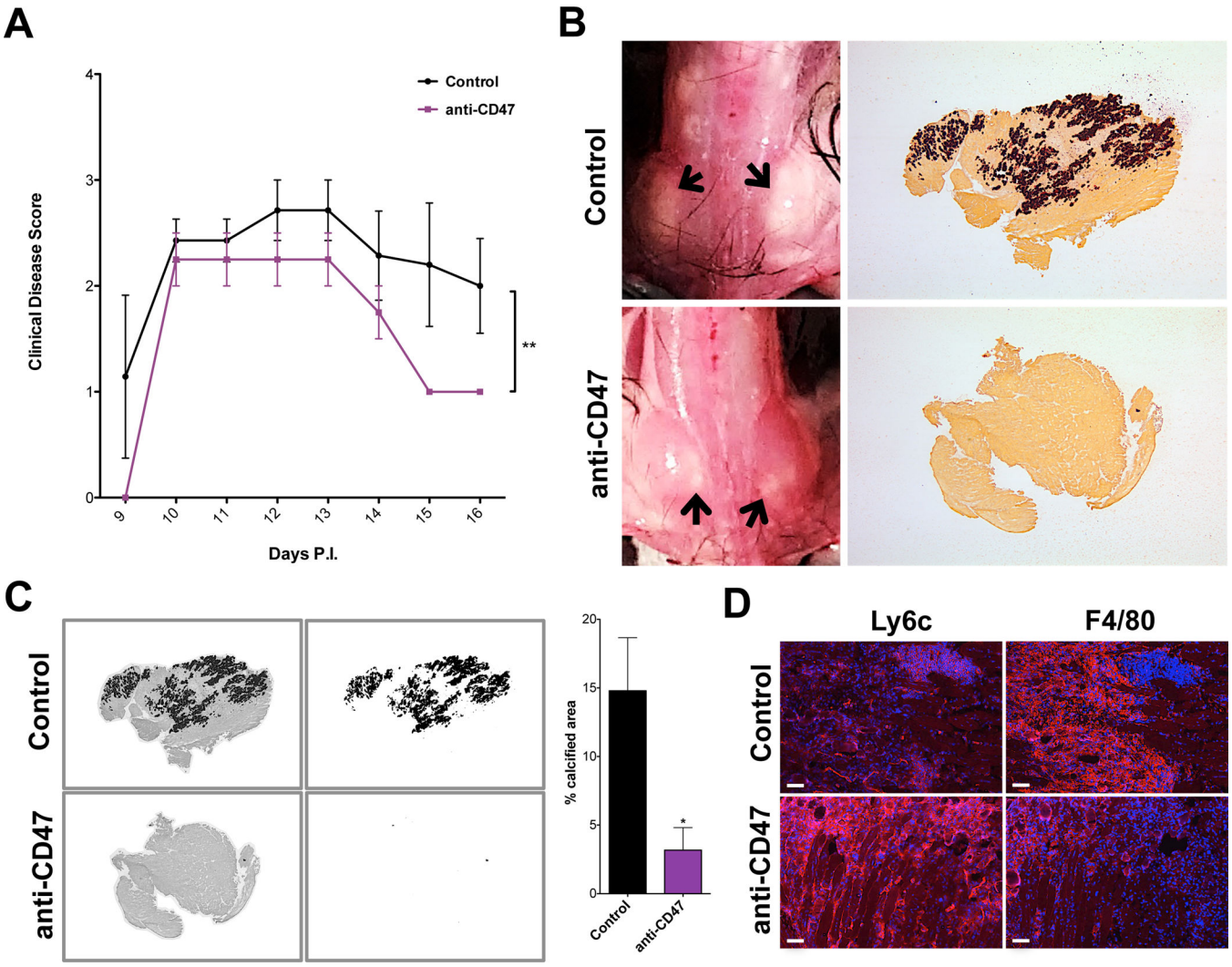

Figure 5. Impact of CD47 neutralization on disease severity

WT BL/6 mice were infected with TMEV and injected with control or CD47-neutralizing antibodies from 5–13 days P.I. (A) Mean clinical disease scores (+/− SEM) of mice according to the following scale: 1) hunched posture and ruffled fur; 2) swollen muscles/ abnormal gait; 3) 1 limb immobilized; 4) 2+ limbs immobilized; 5) death. (B) Muscle calcification observed upon dissection at 16 days P.I. Left panels: representative images of muscle calcification from uninjected and anti-CD47-injected mice; arrows indicate calcified areas. Right panels: representative alizarin red stainings of muscle from uninjected and anti-CD47-injected mice (2× magnification). (C) Percent calcified area of muscle was measured by converting brightfield images of alizarin red stains into 8bit black and white files (left images), measuring the area of dark staining (right images) and measuring the whole tissue area. Representative pictures shown of IgG-injected control and anti-CD47 Ab-injected animals; graph depicts percent calcified area. Uninjected and IgG-injected controls were pooled (n=7); n=3 for CD47-neutralized animals. (D) Frozen muscle from control and CD47-neutralized animals at 16 days P.I. was labeled with antibodies against Ly6c (left) and F4/80 (right) in red and stained with DAPI (blue). Representative images shown of untreated

control and anti-CD47-injected mice; control n=7, anti-CD47 n=4; scale bars depict 100μm; experiment performed in duplicate.

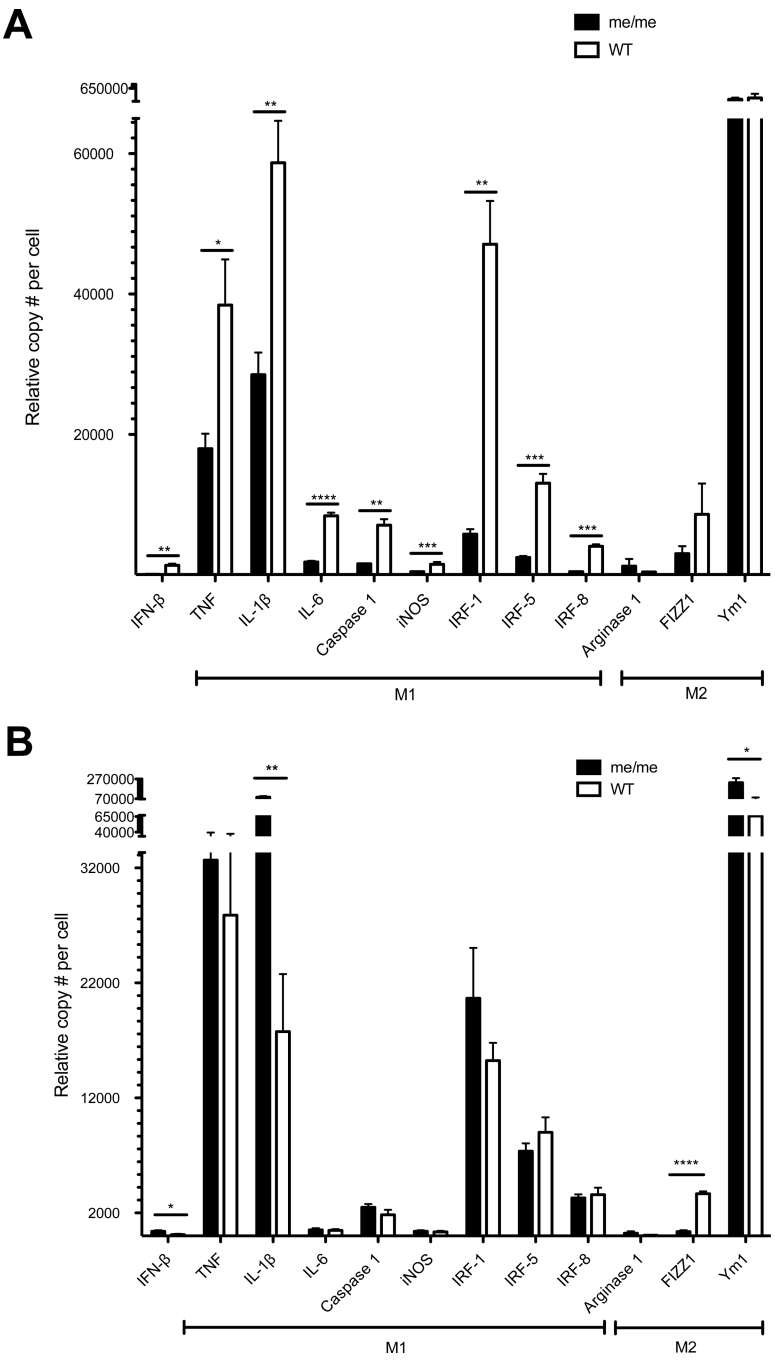

Figure 6. Gene expression in muscle or CNS-infiltrating cells

(A) $CD45^{+}CD11b^{+}Ly6c^{+}$ cells were sorted from skeletal muscle of WT and me/me littermates at 5 days P.I. (B) $CD45^{+}$ cells were sorted from spinal cords of animals shown in (A). (A–B) RNA levels of IFN-β and M1/M2-associated genes were measured using a multiplex bead-based assay. Gene expression levels were normalized to the mean of 3 housekeeping genes (HPRT1, TBP1 and GAPDH) for each sample; n=3.

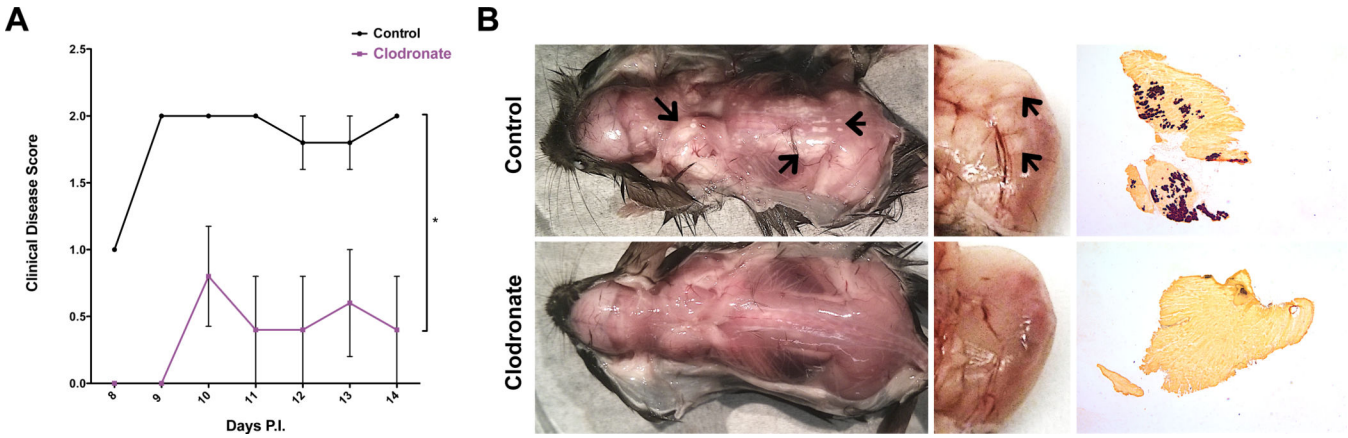

Figure 7. Impact of macrophage depletion on disease severity

WT C3H mice were infected with TMEV and injected with control or clodronate liposomes from 6–12 days P.I. and sacrificed at 14 days P.I.; n=5. (A) Mean clinical disease scores (+/− SEM) of mice according to the following scale: 1) hunched posture and ruffled fur; 2) swollen muscles/abnormal gait; 3) 1 limb immobilized; 4) 2+ limbs immobilized; 5) death. (B) Representative images of muscle calcification observed upon dissection at 16 days P.I., arrows depict examples of calcified areas. Dissection images revealed calcification of whole animals (left), while zoomed images (middle) illustrate calcification of medial gastrocnemius muscle. Representative alizarin red stainings of gluteus maximus muscles shown in right panel (2× magnification).

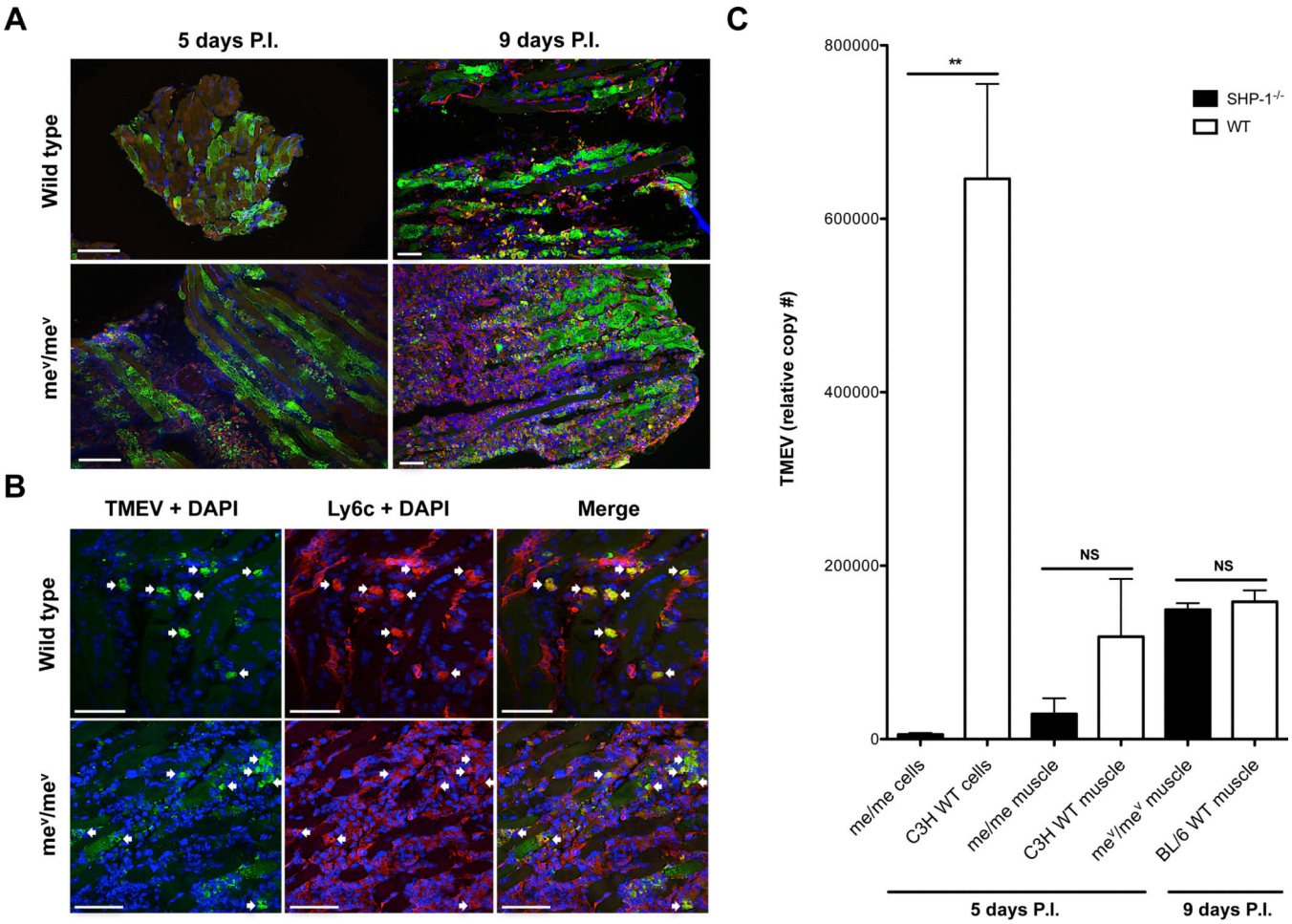

Figure 8. TMEV replication in WT and SHP-1$^{-/-}$ muscle

(A) me^v/me^v mice and wild type littermates were sacrificed at 5 or 9 days P.I. and muscle sections were labeled with TMEV (green) and stained with DAPI (blue); n=3. Sections from animals sacrificed at 5 days P.I. were labeled with antibodies against F4/80 (red), scale bars represent 50μm. Sections from animals sacrificed at 9 days P.I. were labeled with antibodies against Ly6c (red); scale bars represent 100μm. (B) me^v/me^v mice and wild type littermates were sacrificed at 9 days P.I. and muscle sections were labeled with antibodies against Ly6c (red), TMEV (green) and stained with DAPI (blue); arrows suggest infected Ly6c$^+$ cells. Scale bars represent 50μm, n=3. (C) TMEV RNA levels were quantified from CD45$^+$CD11b$^+$Ly6c$^+$ cells sorted from C3H me/me and WT littermates at 5 days P.I. (me/me and C3H WT cells), and homogenized muscle of C3H me/me and WT littermates at 5 days P.I. (me/me and C3H WT muscle) and BL/6 me^v/me^v and WT littermates at 9 days P.I. (me^v/me^v and BL/6 WT muscle). N=3; C3H me/me and WT muscle p=0.1329; BL/6 me^v/me^v and WT muscle p=0.2890.

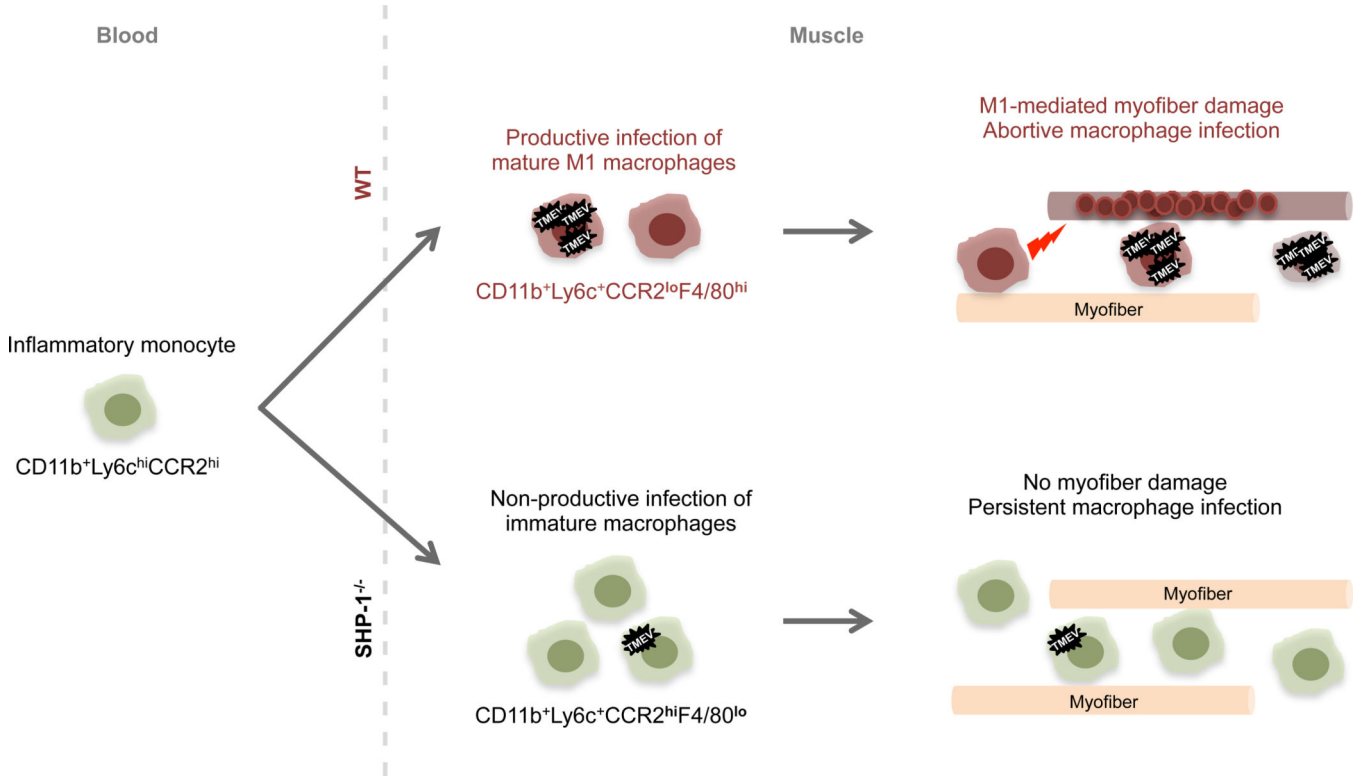

Figure 9. Proposed mechanism of SHP-1-mediated TMEV pathogenesis

Following TMEV infection of skeletal muscle, inflammatory monocytes (green) infiltrate skeletal muscle in WT and SHP-$1^{-/-}$ mice. Top: in WT mice, monocytes differentiate into M1-like macrophages (red), supporting TMEV replication and contributing to muscle fiber damage and subsequent calcification (red circles) likely via proinflammatory cytokines (red lightening bolt). Following active replication TMEV produces an abortive infection, inducing apoptosis of macrophages and limiting the numbers of infiltrating cells. In the absence of SHP-1 (bottom), abnormally high numbers of muscle-infiltrating monocytes remain immature (green), preventing efficient replication of TMEV. These immature monocyte-like cells do not undergo apoptosis and do not produce disease pathology in skeletal muscle.

Table I

Frequency of observed muscle disease in WT and SHP-1$^{-/-}$ mice

	% Mice with observed muscle pathology	P value
C3H[a]		
WT (+/+)	80 (5)	1
WT (+/−)	90.91 (11)	
BL/6[b]		
WT (+/+; +/−)	100 (16)	<0.0001
me^{v}/me^{v}	0 (7)	

Values in parentheses show the number of mice analyzed.

[a] Animals were infected with 6×10^{6} PFU TMEV and sacrificed between 9–15 days P.I.

[b] Animals infected with 6×10^{5} – 3×10^{6} PFU TMEV and sacrificed between 7–11 days P.I.